

Tectonics

RESEARCH ARTICLE

10.1029/2021TC006795

Special Section:

Tethyan dynamics: from rifting to collision

Key Points:

- Subduction interface strength has important role in back-arc stress state
- Back-arc extension in 2D is facilitated by weak overriding plate rheology
- The subduction of narrow oceanic domains can generate enough slab-pull to create back-arc breakup

Supporting Information:

Supporting Information may be found in the online version of this article.

Correspondence to:

Z. Erdős,
zoltan-erdos@staff.elte.hu

Citation:

Erdős, Z., Huisman, R. S., Faccenna, C., & Wolf, S. G. (2021). The role of subduction interface and upper plate strength on back-arc extension: Application to Mediterranean back-arc basins. *Tectonics*, 40, e2021TC006795. <https://doi.org/10.1029/2021TC006795>

Received 2 MAR 2021





Accepted 30 JUN 2021

© 2021. The Authors.

This is an open access article under the terms of the [Creative Commons Attribution-NonCommercial-NoDerivs License](#), which permits use and distribution in any medium, provided the original work is properly cited, the use is non-commercial and no modifications or adaptations are made.



The Role of Subduction Interface and Upper Plate Strength on Back-Arc Extension: Application to Mediterranean Back-Arc Basins

Zoltán Erdős^{1,2} , Ritske S. Huisman³ , Claudio Faccenna^{4,5} , and Sebastian G. Wolf³ 

¹Institute of Earth Physics and Space Science, Eötvös Loránd Research Network, Sopron, Hungary, ²Department of Geophysics and Space Science, Eötvös Loránd University, Budapest, Hungary, ³Department of Earth Sciences, University of Bergen, Bergen, Norway, ⁴Department of Science, University Roma Tre, Roma, Italy, ⁵Jackson School of Geoscience, University of Texas at Austin, Austin, TX, USA

Abstract While there has been a lot of work focusing on improving our understanding of divergent and convergent plate boundaries, the intricate nature of back-arc extension, where subduction and large-scale extension occur and interact in close, is yet to be explored properly. It has long been proposed that the strength of the subduction interface, which depends among others on the amount of subducted sediments, plays a pivotal role in subduction dynamics. Here, we investigate the role of back-arc rheology and subduction interface strength on the deformation style of the overriding plate. Using two-dimensional thermomechanical model experiments, we demonstrate, that the presence of a weak mantle–lithospheric domain in the overriding plate can result in back-arc breakup even during the subduction of narrow, land-locked oceanic basins such as those found in the Mediterranean region. The thinning of the back-arc mantle–lithosphere results in a weaker overriding plate, hence a lower slab-pull force is sufficient to initiate back-arc extension. Convective thinning at the subduction interface also reduces the length of the interface, reducing the portion of slab-pull lost as energy dissipation. A weak plate interface, can also reduce the energy dissipated along the subduction zone, leading to earlier extension. A detailed analysis of the forces shaping the overriding plate stress field shows that transmission of slab-pull force has a predominant role while viscous basal drag has a negligible effect in our experiments. Our results compare favorably with large-scale characteristics of land-locked Mediterranean back-arc basins such as the North Tyrrhenian basin and the Pannonian basin.

1. Introduction

Back-arc basins, such as those behind the island arcs in the Western Pacific Ocean, or those in the Mediterranean region, are common geodynamic systems. They develop on continental or oceanic lithosphere, behind subduction zones due to extensional stress resulting from divergence between trench and upper plate motion. This is most frequently due to subduction rollback, mantle upwelling, or upper plate motion away from the trench (Faccenna et al., 1996, 2014; Le Pichon et al., 1981; Taylor & Karner, 1983).

While abundant research has focused on improving our understanding of both diverging and converging plate boundaries, the dynamics of back-arc extension, where subduction and large-scale extension occur in close, is yet to be fully explored from the perspective of geodynamic processes. For an early example of related studies, see Toksöz and Hsui (1978) who argued early on for the importance of subduction driven convective currents in the formation of back-arc basins. More recently, Arcay et al. (2006) have shown that the dehydration of the subducting slab can result in hydrous weakening and convective removal of the overriding plate mantle–lithosphere, while Currie et al. (2008) argued that back-arc extension can be a result of the extensive thinning of the overriding plate through subduction-induced gravitational instability. Using a 3D approach, Magni et al. (2014) argued for the importance of 3D mantle-flow patterns in producing back-arc extension in the vicinity of continental collision zones. Most recently, Wolf and Huisman (2019) have argued for the importance of not just the overriding plate rheology but also the absolute plate motion velocities in determining the deformation style observed in a back-arc setting.

A key observation regarding continental back-arc basins is that many of them have anomalous high heat flow owing to a thin (~60 km) lithosphere for hundreds of kilometers behind the subduction zone (Currie

& Hyndman, 2006). The origin of such anomalously thin lithosphere is possibly a result of two different mechanisms. The first mechanism is related to subduction-induced small-scale mantle convection that may erode the upper plate mantle–lithosphere (Currie et al., 2008). Another possibility, proposed by Tao and O'Connell (1992), is thinning through ablative subduction, where lithosphere is removed mechanically, by viscous drag from the subducting plate (DeCelles et al., 2009; Sobolev & Babeyko, 2005).

More recently, Wolf and Huismans (2019) showed that the removal of the mantle–lithosphere of the overriding plate through gravitational instabilities is key to produce back-arc extension. Potential examples of the active role of mantle thinning come from several arc–back-arc systems in the Mediterranean area including the Carpathian–Pannonian and Apennine–Tyrrhenian systems. These arc–back-arc systems have narrow, land-locked subducting oceanic basins covered adjacent to the back-arc basin, characterized by the coeval occurrence of anomalously thin back-arc mantle–lithosphere, back-arc extension, slab retreat, and shortening in the overriding plate (Faccenna et al., 2014).

Another factor that has a significant effect on the deformation of the overriding plate is the long-term strength of the subduction interface (e.g., Behr & Becker, 2018; Lamb, 2006). The subduction interface is a zone with many processes acting on both long and short time scales (Angiboust et al., 2011; Cloos & Shreve, 1988a, 1988b; Shreve & Cloos, 1986; Vannucchi et al., 2012). The long-term strength of the subduction interface is thought to be influenced by sediments (Behr & Becker, 2018; Shreve & Cloos, 1986), sea-mounts (Cloos & Shreve, 1988b; Vannucchi et al., 2012), the angle of subduction, and by fluids introduced by dewatering reactions (Vannucchi et al., 2012). The necessity of low-strength plate interfaces in subduction channels has been explored from different points of view in a range of studies (see e.g., De Franco et al., 2007; Sobolev & Brown, 2019, and references therein). In particular, Behr and Becker (2018) showed that the presence of sediments may lubricate the subduction interface resulting in an acceleration of the subducting plate. Lamb (2006) and Lamb and Davis (2003) argued for the role of sediments reducing the shear stresses along the southern Chilean portion of the Andean subduction zone and resulting in significantly lower topographic relief than that of the sediment-starved northern Chilean area. Moreover, a wide range of seismic studies have identified a sedimentary channel unit of 1–8 km thickness along subduction zones (Eberhart-Phillips & Reyners, 1999; Oncken et al., 2003; Tsuru et al., 2002).

Here, we investigate factors controlling the evolution of active back-arc extension in Mediterranean style land-locked oceanic basin settings (Le Pichon, 1982). Many of the extensional back-arc basins in this region presently exhibit a thin mantle–lithosphere and high surface heat flow values. Before the initiation of back-arc extension they were characterized by a slow convergence, driven by the African–European collision and a narrow oceanic basin overlain by a thick sedimentary cover (Jolivet & Faccenna, 2000; Le Pichon, 1982; Le Pichon et al., 1982) and flanked by continental domains (see Faccenna et al., 2014, and references therein). Such narrow oceanic basins can only produce a limited amount of slab-pull before their closure, making back-arc extension particularly difficult to achieve.

For example, the North Tyrrhenian Sea (Figure 1b (Diaferia et al., 2019; Doglioni et al., 1999; Piana Agostinetti & Faccenna, 2018) exhibits moderately thinned back-arc crust (20–30-km thick) in an approximately 100-km-wide region adjacent to the subducting Adriatic slab. In contrast, the mantle–lithosphere of the backarc is extremely thinned with anomalously high Moho temperatures and *P* wave tomography suggesting very thin to absent mantle–lithosphere (Diaferia et al., 2019; Di Stefano et al., 2009), while seismic receiver function analysis data point to an LAB depth of 60 km below the North Tyrrhenian basin (Miller & Piana Agostinetti, 2012).

Another Mediterranean back-arc basin, the Pannonian basin (Figure 1a) was formed during the rapid roll-back of the Carpathian slab between 20 and 9 Ma (e.g., Balázs et al., 2016; Csontos et al., 1992; Fodor et al., 1999; Horváth et al., 2006; Matenco & Radivojević, 2012; Schmid et al., 2008). The slab imaged through seismic tomography below the East Carpathian Vrancea zone is approximately 500 km long. A peculiar feature of this backarc is the nonextensional Transylvanian basin in the eastern part Carpathian embayment (Ciulavu et al., 2001) of which the formation is poorly understood (Horváth et al., 2006). L. H. Royden et al. (1982) proposed that it was formed as a continental sag caused by the suction force exerted to the overriding plate by the Carpathian slab. The Transylvanian basin and the Apuseni Mountains that

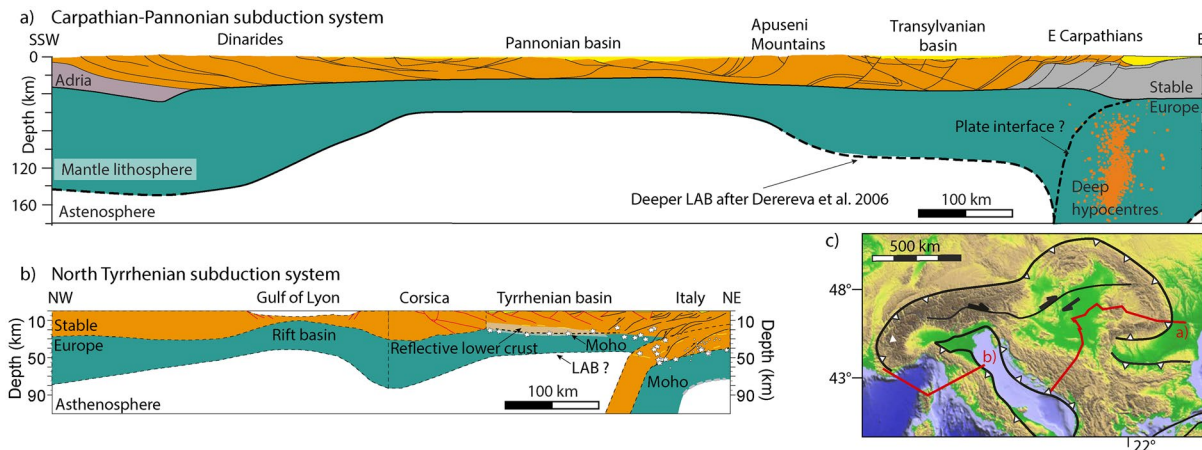


Figure 1. (a) Lithospheric scale cross section in over the Dinarides–Pannonian basin–Apuseni Mountains–Transylvanian basin–East Carpathians edited after Balázs et al. (2016). (b) Lithospheric scale cross section along the CROP-3 transect in the North Tyrrhenian Sea edited after Faccenna et al. (2001), Piana Agostinetti and Faccenna (2018), and Doglioni et al. (1999). The LAB was drawn based on Suhadolc et al. (1990). (c) Map showing the traces of the presented cross sections, edited from Balázs et al. (2016).

separate it from the rest of the Pannonian basin have also experienced less thinning and have a markedly thicker lithospheric root.

In this study, we use two-dimensional numerical model experiments to investigate how overriding plate rheology and strength of the subduction interface affect the closure of narrow land-locked oceanic basins like the ones described above and the opening of back-arc extensional basins. In the models presented here, we vary the strength of the overriding plate mantle–lithosphere and explore the effect of the presence or absence of a weak subduction interface.

2. Numerical Method

2.1. Model Description

We use a modified version of the 2D finite element thermomechanical numerical model FANTOM (Thieulot, 2011; Wolf & Huisman, 2019). This code solves the Stokes equation coupled to the heat transport equation in 2D, using the plane strain assumption where the mechanical and thermal systems are coupled through temperature-dependent rheologies and densities and are solved sequentially for each model time step. In this latest version of the code adiabatic heating, temperature-dependent conductivity and P–T-dependent phase changes have been implemented. We model thermomechanically coupled, incompressible viscous–plastic creeping flows. The densities of the modeled materials depend on temperature: $\rho(T) = \rho_0(1 - \alpha(T - T_0))$, with the thermal expansion coefficients α and the reference densities at temperature $T_0 = 0^\circ\text{C}$ given in Table 1. For mantle materials, the thermal expansion coefficients are P–T dependent with a linear increase from 3×10^{-5} to $4 \times 10^{-5} \text{ K}^{-1}$ in the temperature range of 500–2,000 K and a linear decrease by a factor 1–0.5 from 0 to 45 GPa (Agrusta et al., 2017; Butler et al., 2015; Tosi et al., 2013). For the sublithospheric mantle, and the constant viscosity lower mantle, in order to mimic active mantle convection at high Nusselt number, the conductivity linearly increases from 2.25 to $52.0 \text{ W m}^{-1} \text{ K}^{-1}$ in the temperature range of $1,335^\circ\text{C}$ – $1,345^\circ\text{C}$. This approach has been widely used in subduction as well as rift modeling studies (Butler & Beaumont, 2017; Pysklywec & Beaumont, 2004; Tetreault & Buitier, 2012; Warren et al., 2008) as it prevents secular cooling of the model domain while maintaining a constant vertical heat flux at the base of the lithosphere and keeping the mantle close to the adiabatic gradient.

When stress is below yield, deformation occurs by viscous flow and follows temperature-dependent nonlinear power law rheologies. The effective viscosity η_{eff} is specified as

$$\eta_{\text{eff}} = fA^{-1/n} \dot{\epsilon}_{\text{II}}^{(1-n)/2n} \exp\left(\frac{Q + Vp}{nRT}\right) \quad (1)$$

Table 1
Material Properties

Units	Materials										
	Continental plate				Oceanic plate				Asthenosphere		
	Sediment cover	Upper crust (pro)	Lower crust	Mantle–lithosphere	Crust	Mantle–lithosphere	Eclogite from sediment	Eclogite from crust	Sublithospheric mantle	Lower mantle	Slab in the lower mantle
Mechanical parameters											
Thickness (km)	4 (0 or 2) ^a	24	12	84	9 (7) ^b	71	–	–	536 (580) ^c	740	–
ρ_0 (kg m ⁻³)	2,800	2,800	3,000	3,380 (3,360) ^d	2,900	3,380 (3,365) ^e	3,365	3,380	3,380	3,630	3,630
φ – φ_{sw} (°)	8–2	15–2	15–2	15–2	7–1	15–2	15–2	15–2	15–2	–	15–2
C – C_{sw} (Pa)	2×10^7 to 4×10^6	2×10^7	2×10^7	2×10^7	2×10^7	2×10^7	2×10^7 to 4×10^6	2×10^7	2×10^7	–	2×10^7
Flow law	WQ ¹	WQ ¹	DMD ²	WO ³	DMD ²	WO ³	WQ ¹	DMD ²	WO ³	–	WO ³
scaling factor	1	1 (5) ^f	0.1	5 (0.2) ^g	0.1	5	0.5	0.1	1	–	5
A (Pa ^{-n} s ⁻¹)	8.574×10^{-28}	8.574×10^{-28}	5.78×10^{-27}	1.76×10^{-14}	5.78×10^{-27}	1.76×10^{-14}	8.574×10^{-28}	5.78×10^{-27}	1.76×10^{-14}	–	1.76×10^{-14}
Q (J mol ⁻¹)	2.228×10^5	2.228×10^5	4.85×10^5	4.3×10^5	4.85×10^5	4.3×10^5	2.228×10^5	4.85×10^5	4.3×10^5	–	4.3×10^5
N	4	4	4.7	3	4.7	3	4	4.7	3	–	3
V (m ³ mol ⁻¹)	0	0	0	1.1×10^{-5}	0	1.1×10^{-5}	0	0	1.1×10^{-5}	–	1.1×10^{-5}
Thermal parameters											
c_p (m ² K ⁻¹ s ⁻²)	750	750	750	1,250	750	1,250	750	750	1,250	1,250	1,250
k (W m ⁻¹ K ⁻¹)	2.25	2.25	2.25	2.25	2.25	2.25	2.25	2.25	2.25–52.0	2.25–52.0	2.25
α (K ⁻¹)	3×10^{-5}	3×10^{-5}	3×10^{-5}	3×10^{-5} to 4×10^{-5}	3×10^{-5}	3×10^{-5} to 4×10^{-5}	3×10^{-5}	3×10^{-5}	3×10^{-5} to 4×10^{-5}	3×10^{-5} to 4×10^{-5}	3×10^{-5} to 4×10^{-5}
H (μW m ⁻³)	1.1×10^{-6}	1.1×10^{-6}	5×10^{-7}	0	0	0	0	0	0	0	0
η range					10^{19} to 10^{27}					2×10^{21}	10^{19} to 10^{27}

Note. WQ, wet quartz flow law described by Gleason and Tullis (1995); DMD, dry Maryland diabase flow law described by Mackwell et al. (1998); WO, wet olivine flow law described by Karato and Wu (1993).

^aValue in parentheses shows the thickness of sediments on top of the oceanic crust. ^bValue in parentheses shows the thickness of oceanic crust in the presence of a sedimentary layer on top of it. ^cValue in parentheses shows the thickness of the sublithospheric mantle under the undeformed oceanic lithosphere. ^dValue in parentheses shows the density of the depleted layer of continental mantle–lithosphere. ^eValue in parentheses shows the density of the depleted layer of oceanic mantle–lithosphere. ^fValue in parentheses shows the value of the scaling factor applied for the procontinental upper crust (see text for details). ^gValue in parentheses shows the scaling factor applied for the weakened portion of the continental mantle–lithosphere.

where A is the pre-exponential scaling factor, n is the power law exponent, ε_{II} is the second invariant of the deviatoric strain-rate tensor, Q is the activation energy, V is the activation volume, p is the pressure, T is the temperature, and R is the universal gas constant. Values for the parameters A , n , Q , and V are based on laboratory measurements carried out on “wet” olivine, “wet” quartzite, and dry Maryland diabase (Gleason & Tullis, 1995; Karato & Wu, 1993; Mackwell et al., 1998). Values used for the modeled materials are given in Table 1. The effective viscosity of quartz-dominated rocks is characterized by large uncertainties due to compositional differences (Huismans & Beaumont, 2011) while laboratory data show that water-saturated olivine is 5–20 times weaker than dehydrated olivine at the same strain rate (Hirth & Kohlstedt, 1996; Karato & Wu, 1993). We use a scaling factor (f) to approximate the effect of variations in volatile content and potential changes in strength due to minor compositional variations (e.g., Beaumont

et al., 2006). The dry Maryland diabase rheology of the continental lower crust and oceanic crust is scaled downward ($f = 0.1$), as the laboratory diabase was drier, and consequently stronger, than typical lower crust (e.g., Currie et al., 2008).

Frictional-plastic yielding is modeled with a pressure-dependent Drucker–Prager yield criterion, equivalent to the Coulomb yield criterion in two dimensions. Yielding occurs when

$$\left(J_2'\right)^{1/2} = p \sin \phi_{\text{eff}} + C \cos \phi_{\text{eff}} \quad (2)$$

where J_2' is the second invariant of the deviatoric stress, ϕ_{eff} is the effective internal angle of friction (that includes the effect of pore-fluid pressure), and C is cohesion. With appropriate choice of C and ϕ_{eff} , this yield criterion approximates the effect of pore-fluid pressure and frictional sliding in rocks. Mechanisms such as fluid-pressure variations (Sibson, 1990), grain-size reduction, and mineral transformations (Bos & Spiers, 2002) may reduce the frictional strength. The effect of these frictional-plastic strain-softening mechanisms is introduced into the model through a linear decrease of the internal angle of friction from 15° to 2° and—for the sedimentary layers—a simultaneous decrease of cohesion from 20 to 4 MPa as the second invariant of deviatoric strain varies from 0.4 to 1.4 (Figure 1b). We note that $\phi_{\text{eff}}(\varepsilon) \approx 15^\circ$ corresponds to the effective friction angle when the pore-fluid pressure is approximately hydrostatic.

2.2. Initial and Boundary Conditions

The initial temperature field is defined uniformly for the continental and the oceanic domains. We use this to avoid artificially high-temperature gradients that would appear at the transition from the warmer oceanic lithosphere to the colder continental lithosphere. The initial temperature profile increases with depth from the surface ($T_0 = 0^\circ\text{C}$) to the base of the crust ($T_m = 550^\circ\text{C}$), and to the base of the lithosphere ($T_{\text{lab}} = 1,330^\circ\text{C}$) from where it adiabatically increases to the base of the model domain ($T_{\text{base}} = 1,850^\circ\text{C}$). The bottom and surface boundaries are kept at a constant temperature, while the side boundaries are thermally insulated.

Velocity boundary conditions are imposed on both sides of the model with initially a constant convergence velocity ($v_{\text{conv}} = 5 \text{ cm year}^{-1}$) imposed on the lithosphere on the left side of the model while the right side is kept fixed. After 6 Myr, this convergence velocity is reduced to $v_{\text{conv}} = 1 \text{ cm year}^{-1}$. The initial 5 cm year^{-1} value allows for the development of a slab that can exert a pulling force on the oceanic lithosphere. Finally, for each individual model experiment, $v_{\text{conv}} = 0 \text{ cm year}^{-1}$ is set after the oceanic basin is fully consumed, to mimic a soft docking, where the far-field forcing is diminished in sync with the start of collision. The time of this transition varies from model to model: the shortest convergence period is 10 Myr in case of Model 4 while the longest is 31 Myr in case of Models 1 and 3. This setup allows us to focus on the precollisional evolution of these arc–back-arc systems.

The velocities in the sublithospheric upper mantle are defined so that the material influx and outflux through the lateral boundaries are in balance at any given time. In the constant viscosity lower mantle, the side boundaries are closed. At the base of the model, a free-slip condition is imposed. There is no material-transport through this boundary. In order to restrict the effects of the slab's interference with the bottom boundary of the model, the slab is arbitrarily transformed into lower-mantle material at 1,300 km depth. The use of the arbitrary Lagrangian–Eulerian grid-setup allows for a free-surface at the top of the model.

2.3. Model Setup

Inspired by the Mediterranean style land-locked oceanic basins (e.g., Le Pichon, 1982), the model is represented by an oceanic plate enclosed by two continental plates (Figure 2). The model domain is 3,000-km wide and 1,400-km deep, so that the modeled lithospheric plates sit on top of an adiabatic upper mantle and a linear-viscous lower mantle. The lithospheric domain is divided in the middle by a boundary dipping 45° to the right. At this divide, the model is seeded with an inclined, strain-weakened oceanic crustal domain underneath the retrocontinent to allow for initiation of oceanic subduction.

The oceanic lithosphere is 500-km wide and is bounded by a narrow, steeply dipping passive continental margin. The continental domain on the left side of the model is considered the procontinent and consists of

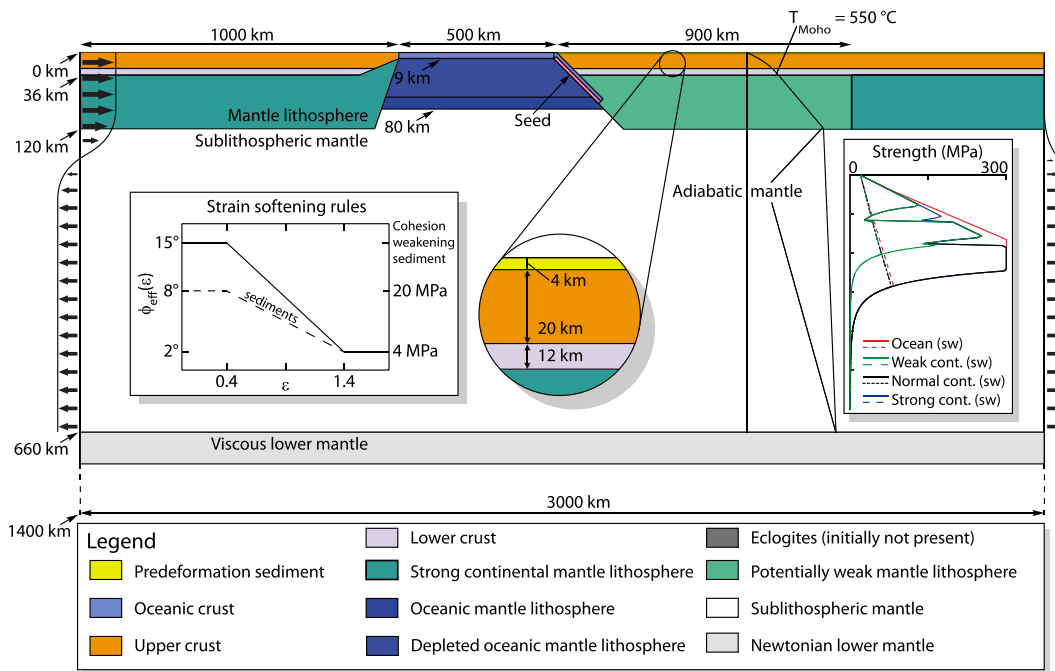


Figure 2. Numerical model design, showing (1) the experimental layout, (2) the velocity boundary conditions, (3) the strain-softening rules, (4) the initial temperature field, and (5) the initial strength profiles. The legend identifies the different material types used. For the material properties, of each material type, see Table 1.

a 24-km-thick upper crust, a 12-km-thick lower crust, and an 84-km-thick continental lithospheric mantle. The continental domain on the right side of the model is the retrocontinent and has the same material setup as the procontinent but the top 4 km of the upper crust is made up of a weaker layer representing sediments. The upper crust of the procontinent is 5 times stronger than that of the retrocontinent in order to prevent the front-end of the procontinent from being wrenched off by the fully subducted slab.

The oceanic domain consists of a 9-km-thick oceanic crust and a 71-km-thick oceanic lithospheric mantle of which the top 60 km is 15 kg m^{-3} depleted. In the second set of models, the top 2 km of the oceanic crust is replaced by a sedimentary layer. With this rheological parametrization, the subducting oceanic lithosphere has a mild negative buoyancy in the constant viscosity lower mantle, but the arising force is balanced by the higher viscous drag. Hence, when the slab-pull force is calculated we only take into account the portion of the slab that is in the upper mantle.

Underneath the lithospheric mantle, a sublithospheric mantle extends to 660 km depth. The bottom layer of the model is a constant viscosity lower mantle. The specific material properties for each material can be found in Table 1.

Upon reaching the right temperature–pressure conditions, the oceanic crust and—if present—the oceanic sediments are automatically transformed into eclogite (Hacker, 1996). Eclogite has the same viscous flow law as the oceanic crust but a different density. In order to keep the models simple, we assume that sediments obtain a higher, metamorphic density when entering the eclogite stability field. All slab and mantle materials are subject to a reversible phase change at the 660-km discontinuity, corresponding to the breakdown of ringwoodite to bridgmanite and magnesiowüstite (see discussion in Billen [2010] and Goes et al. [2017]). For simplicity, all the different materials that make up the slab are converted to one lower-mantle slab material, which has the viscous flow law of the oceanic lithosphere. The phase changes do not account for latent heat and are not mass conserving and capture the first-order effects of important metamorphic phase changes (Wolf & Huismans, 2019).

The Eulerian grid consists of 1,250 cells in the horizontal direction (giving a resolution of 2.4 km) and 257 cells in the vertical direction. The vertical resolution is irregular, with 127 elements covering the bottom

1,270 km of the model (giving a vertical resolution of 10 km), while the remaining 130 elements located in the top 130 km of the model (giving a vertical resolution of 1 km). The grid refinement was used to increase the resolution in the lithosphere but attain a reasonable computation time.

2.4. Post Processing

We discuss the results of our models using force-balance arguments. For each model, we calculate and present the time-evolution of the slab-pull force and the far-field forcing.

The slab-pull force results from the negative buoyancy of the downgoing slab relative to its surroundings. We calculate the evolving slab-pull force in the models by tracking the cells containing the slab in the 135–660-km depth range at each time step. We take a reference density profile of this depth range at the left side boundary and for each cell containing slab material (i.e., sediment, oceanic crust, oceanic and continental lithosphere, and serpentinites), we calculate the density difference from the reference density profile at its corresponding depth and then integrate the resulting density difference (multiplied by the gravitational constant).

The far-field forcing on each side is calculated by integrating the horizontal deviatoric stress in the lithosphere at the edges of the model domain. For each cell containing lithospheric material, we track the effective viscosity and horizontal component of the strain-rate tensor and calculate the local horizontal deviatoric stress as $\tau_{xx} = 2\eta_{\text{eff}}\dot{\epsilon}_{xx}$ before integrating with depth.

3. Results

Here, we present two sets of numerical experiments with three models each. In both sets, the rheology of the retrocontinental mantle–lithosphere is varied in the same manner (i.e., uniformly strong; 600-km-wide weak zone adjacent to subduction zone; 600-km-wide weak zone 300 km away from the subduction zone). The difference between the model sets is the presence (in set 2) of a 2-km-thick low-strength, cohesion-weakening sedimentary layer on top of the oceanic lithosphere.

3.1. Model 1: Reference Model

The reference model (Figure 3, Supporting information Figure S1, and Supporting information Animation 1) has a uniformly strong back-arc lithospheric mantle. In this model, the oceanic domain subducts in a stable manner as the retrocontinent remains undeformed throughout the entire model run. The oceanic basin is closed by about 25 Myr, when the upper crust of the procontinent enters the subduction channel. The convergence is stopped at 31 Myr to achieve soft docking. At this point, the oceanic slab is hanging vertically in the sublithospheric mantle (Figure 3a). Subsequently, the slab weakens as it heats up conductively and eventually breaks off in two phases; first, at 52.5 Myr model time at about 375 km depth (Figure 3b) and then at around 76 Myr model time at 200 km depth (Figure 3c).

The evolution of the slab-pull force and the tectonic forcing on the two side boundaries (approximated by the cumulative shear-stress on the sides of the lithosphere) is tracked in Figure 3d. Initially, the slab-pull force builds up rapidly until the convergence is slowed down at 6 Myr. From here on the buildup is slower until the convergence is fully stopped at 31 Myr (at value of $1.5 \times 10^{13} \text{ N m}^{-1}$). After this point, the gradual conductive heating of the slab reduces its negative buoyancy while the two slab break-off events eventually reduce its value to zero.

Tracking the forces on the side boundary also shows us how the fixed velocity boundaries drive the model initially before the slab-pull force takes over at around 6 Myr model time (at the time the tectonic forcing curves cross from the compressional to the tensional domain). Their values remain relatively stable at approximately $0.2 \times 10^{12} \text{ N m}^{-1}$ until the convergence is stopped. At this point, the boundary force magnitudes increase to approximately $0.25 \times 10^{12} \text{ N m}^{-1}$ to compensate for the loss of the driving force from the sides and then slowly diminish with the decrease of slab-pull force until they finally reach a value near zero at the first slab break-off event.

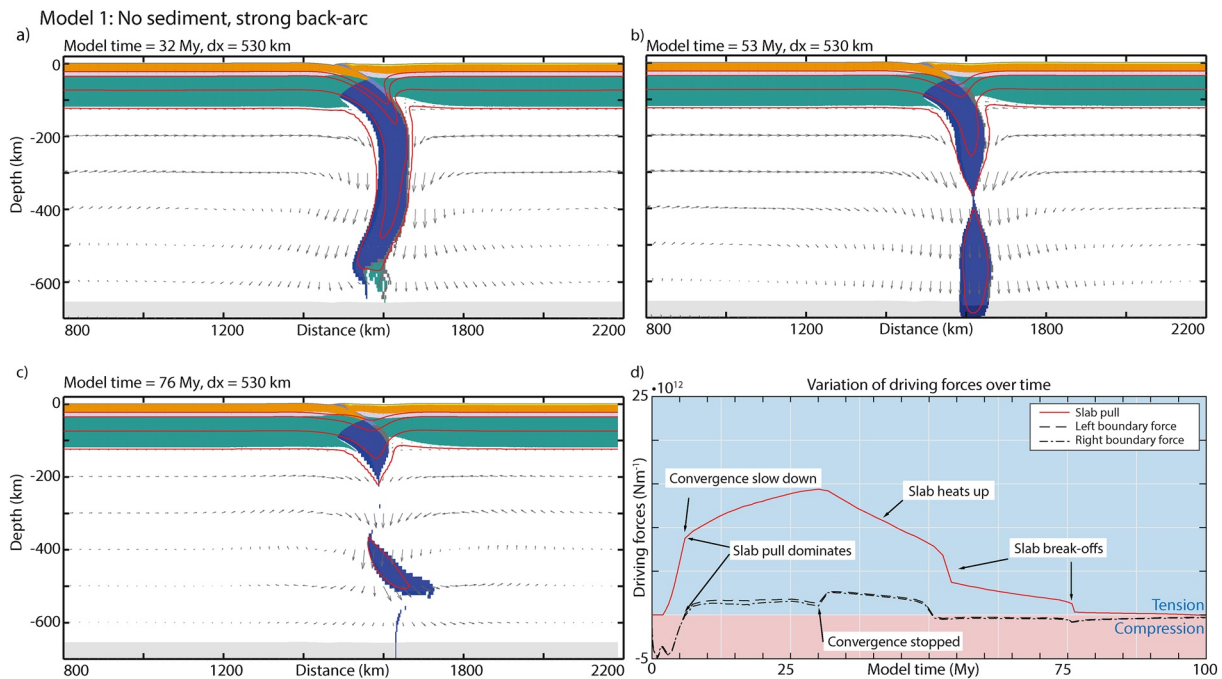


Figure 3. Reference model (Model 1) showing clean subduction and no back-arc deformation. (a–c) Material colors (see Figure 1 and legend there) of key time steps, with isotherms (red lines: 420°C, 550°C, 900°C, and 1,330°C) and advection velocities (gray arrows; lengths scale with velocities). (d) Driving force estimates throughout the model run.

The above described force plot clearly shows that even though the slab-pull force becomes dominant early on, the tensional force transferred to the right edge of the model (black dashed-dotted line) stays low ($<3 \times 10^{12} \text{ N m}^{-1}$) throughout the model run (Figure 3d). The tensional force never becomes high enough to overcome the integrated strength of the backarc ($\sim 8.5 \times 10^{12} \text{ N m}^{-1}$).

3.2. Model 2: Weak Backarc

In Model 2, the retrocontinental mantle–lithosphere is modified, so that a 600-km-wide zone immediately behind the subduction interface is weakened by a factor of 20 (Figure 4, Supporting information Figure S2, and Supporting information Animation 2). Note that the weakening is only applied after 2 Myr so it does not interfere with the subduction initiation phase.

The difference from the behavior observed in the reference model is pronounced, as the back-arc mantle–lithosphere is removed both convectively and ablatively. This rapid thinning of the backarc weakens the lithosphere, and eventually the pull, exerted by the retreating slab overcomes the strength of the retrocontinent. The back-arc crust starts extending in a pure-shear mode (i.e., in a vertically quasi homogenous manner) around 10 Myr (when the tip of the slab is at about 420 km depth; Figure 4a) and the system reaches back-arc breakup by 13 Myr. The rollback of the subducting plate driven by slab-pull results in the consumption of the entire oceanic basin by the time of full crustal breakup in the backarc. To achieve soft docking, the convergence is stopped at 13 Myr model time (Figure 4b).

Full lithospheric breakup—represented by a mildly asymmetric rift—occurs approximately 200 km behind the subduction zone. After breakup, the portion of the backarc still attached to the overriding plate stops extending (apart from the continued convective removal of its mantle–lithosphere) while the portion separated by the rift from the rest of the overriding plate collides with the incoming procontinent, moving approximately 140 km in 0.7 Myr. The drift of this arc gradually slows down and eventually stops entirely by 15.7 Myr (see Supporting information Animation 2). At this point, the entire initial oceanic basin is subducted with upper-crustal material filling out the subduction channel. Behind the arc sits an approximately 180-km-wide oceanic rift-basin. The oceanic slab breaks off around 17.3 Myr (Figure 4c). The leading edge

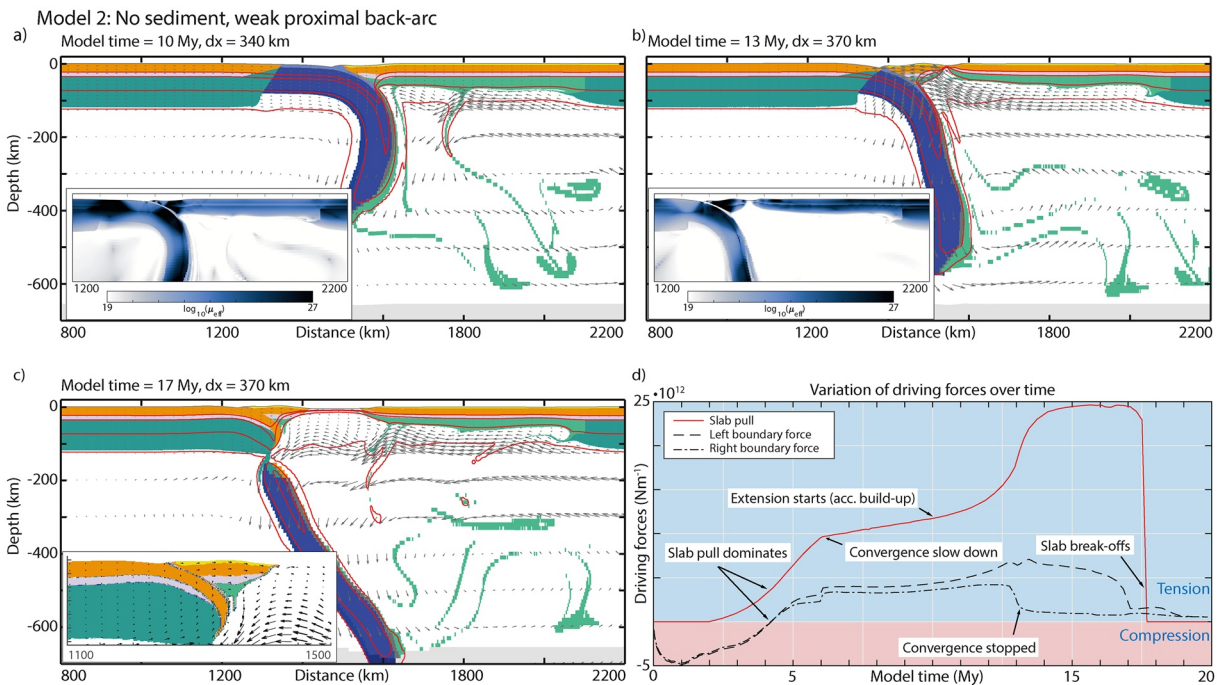


Figure 4. Weak back-arc model (Model 2) showing back-arc spreading. (a–c) Material colors (see Figure 1 and legend there) of key time steps, with isotherms (red lines: 420°C, 550°C, 900°C, and 1,330°C) and advection velocities (gray arrows; lengths scale with velocities). (d) Driving force estimates throughout the model run.

of the procontinent and the approximately 200-km-wide lithospheric block that has been rifted off the overriding plate experiences a rapid phase of uplift and retrograde drift, moving toward the stable overriding domain (see inset of Figure 4c).

Like in Model 1, the evolution of the driving forces through the experiment is presented in Figure 4d. The slab-pull force builds up relatively fast to a value of $1 \times 10^{13} \text{ N m}^{-1}$ by the time the imposed convergence velocity is lowered to 1 cm year^{-1} . From here on, the slab-pull builds up slowly but when it reaches a value of approximately $1.2 \times 10^{13} \text{ N m}^{-1}$ at around 10 Myr the backarc starts extending. This allows for the slab to roll back and the slab-pull force to build up increasingly fast, especially after the convergence is stopped at 13 Myr. The slab-pull force reaches a plateau at a value of $2.5 \times 10^{13} \text{ N m}^{-1}$ before the slab breaks off. The stresses measured on the sides of the model show that initially a significant far-field force (up to $5 \times 10^{12} \text{ N m}^{-1}$ in the compressional domain) is required to drive the convergence before the slab-pull starts dominating the system already at 4 Myr model time. The stresses measured along the side boundaries stabilize at around $4.5 \times 10^{12} \text{ N m}^{-1}$ before the right boundary force drops down to a value around zero at 13 Myr while the left boundary force increases to approximately $7 \times 10^{12} \text{ N m}^{-1}$. This divergence coincides with the back-arc rifting. Finally, the left boundary force also drops to zero around the time the slab breaks off.

3.3. Model 3: Weak Distal Backarc

In Model 3, the back-arc lithospheric mantle is weakened in a 600-km-wide zone, but 300 km away from the subduction interface (Figure 5, Supporting information Figure S3, and Supporting information Animation 3). Weakening is only applied after 2 Myr so it does not interfere with the subduction initiation phase.

Similarly to Model 2, the weakened mantle–lithosphere is progressively removed in a convective manner (Figure 5a). However, there is no significant ablative removal of the weak mantle–lithosphere as it is not in direct contact with the subducting slab. Mantle wedge lithospheric thinning is limited, and the length of the subduction interface (measured from the trench to the LAB) remains virtually constant throughout the model run. Even though the weak portion of the back-arc lithospheric mantle is thinned and the continental crust on top experiences corresponding heating up (Moho temperature exceeding 750°C) there is no

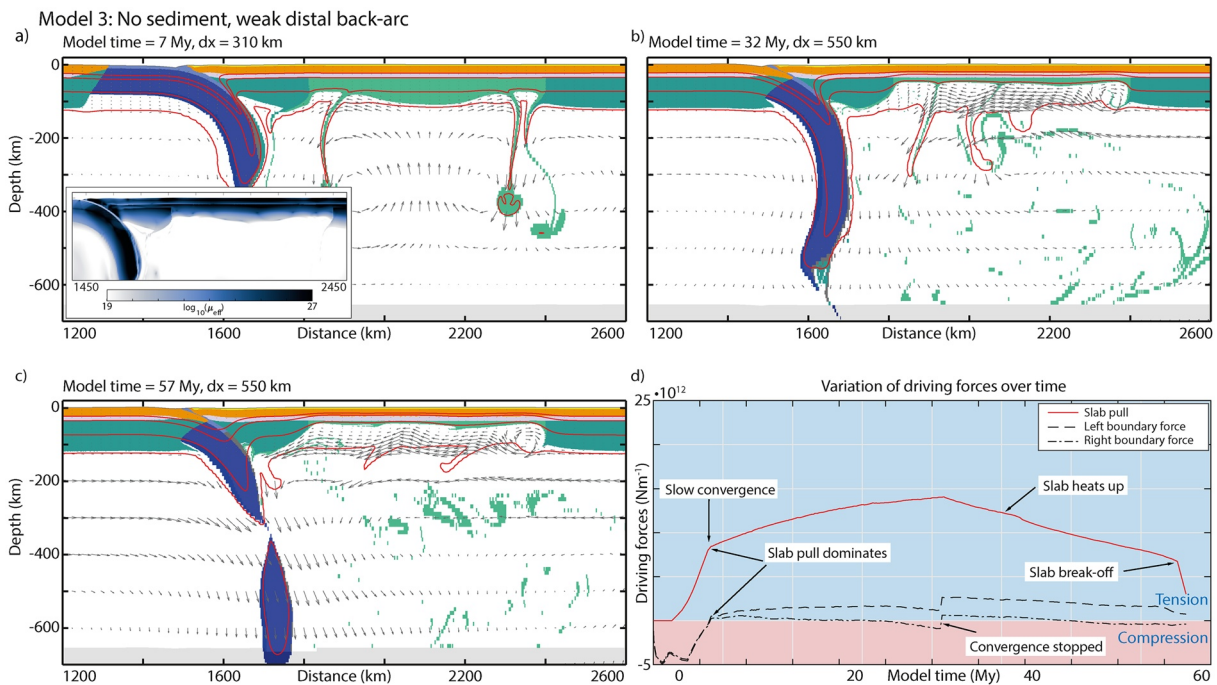


Figure 5. Weak distal back-arc model (Model 3) showing back-arc thinning without crustal breakup. (a–c) Material colors (see Figure 1 and legend there) of key time steps, with isotherms (red lines: 420°C, 550°C, 900°C, and 1,330°C) and advection velocities (gray arrows; lengths scale with velocities). (d) Driving force estimates throughout the model run.

back-arc breakup and no trench retreat. The continental crust above the weak domain in the retrocontinent is remarkably free of internal deformation.

The convergence is stopped at 31 Myr and by this time the oceanic lithospheric slab is in a vertical position below the procontinent (Figure 5b). Finally, at around 57.3 Myr model time, the slab breaks off at 300 km depth (Figure 5c).

The evolution of the driving forces is plotted in Figure 5d. The evolution of the slab-pull force is largely identical to that of Model 1 (Figure 3d; note the different time scale). The low values of the left boundary force are also concordant with the values observed in Model 1 suggesting a similar balance between the far-field forcing provided by the constant velocity boundary condition and the slab-pull force. The near zero values of the forces measured along the right-hand side boundary of the model infer a system where there is almost no force left to be transferred to the backarc, even though the strength of the overriding plate is significantly lowered by the convective removal of its mantle–lithosphere (Figure 5d).

3.4. Model 4: Strong Backarc and Weak Plate Interface

Set 2 (Models 4–6) consists of the same three model setup as in set 1 (Models 1–3), but instead of a 9-km-thick oceanic crust, the top of the oceanic domain comprises a 2-km-thick, weak sedimentary layer overlying a 7-km-thick oceanic crust.

The presence of the oceanic sedimentary layer weakens coupling at the subduction interface between the oceanic lithosphere and the overriding plate. In case of a strong back-arc lithosphere (Model 4), this results in almost no discernible difference from the large-scale behavior observed in Model 1. The oceanic domain is subducted without major deformation of the overriding plate (Figure 6, Supporting information Figure S4, and Supporting information Animation 4) before the soft docking of the incoming continent at 31 Myr model time (Figure 6a). This is followed by a similar two-phase slab break-off as observed in Model 1.

The evolution of the driving forces is plotted in Figure 6d. The evolution of the slab-pull force is largely identical to that of Model 1 (Figure 3d). The evolution of the tectonic forcing measured on the side boundaries

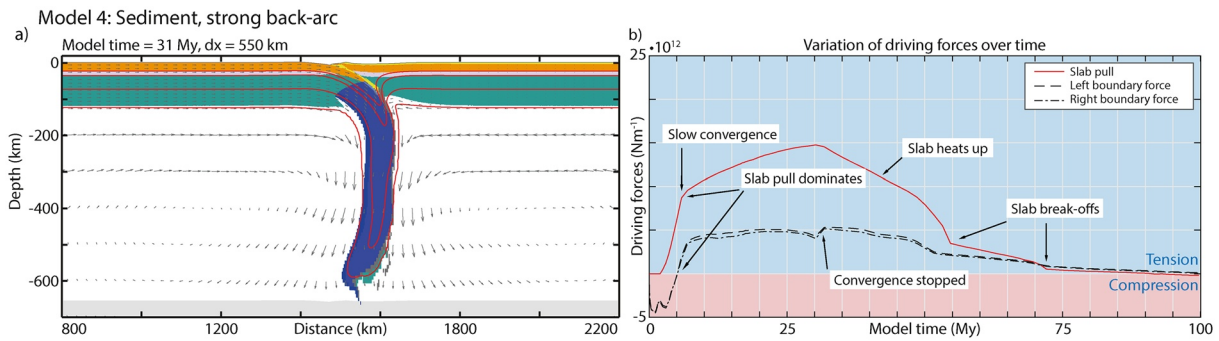


Figure 6. Reference model with oceanic sediments (Model 4) showing clean subduction. (a) Material colors (see Figure 1 and legend there) of key time steps, with isotherms (red lines: 420°C, 550°C, 900°C, and 1,330°C) and advection velocities (gray arrows; lengths scale with velocities). (b) Driving force estimates throughout the model run.

is also similar, but the values reach up to $5 \times 10^{12} \text{ N m}^{-1}$ when the system is dominated by slab-pull. These increased values point to less energy dissipation along the slab interface. The high tensional force measured along the right boundary of the model also infers an efficient transfer of the slab-pull force into the overriding plate, but it is not enough to overcome the integrated strength of the overriding plate that remains high in the absence of convective thinning of its mantle–lithosphere.

3.5. Model 5: Weak Backarc and Weak Plate Interface

Similarly, the model with a weakened back-arc zone adjacent to the subduction interface exhibits a largely identical behavior regardless of the presence (Model 5; Figure 7, Supporting information Figure S5, and Supporting information Animation 5) or absence (Model 2; Figure 4) of an oceanic sedimentary layer. In case of Model 5, however, the backarc starts extending significantly earlier, at around 6.6 Myr, when the slab reaches a depth of approximately 395 km (Figure 7a and Supporting information Animation 5), leading to

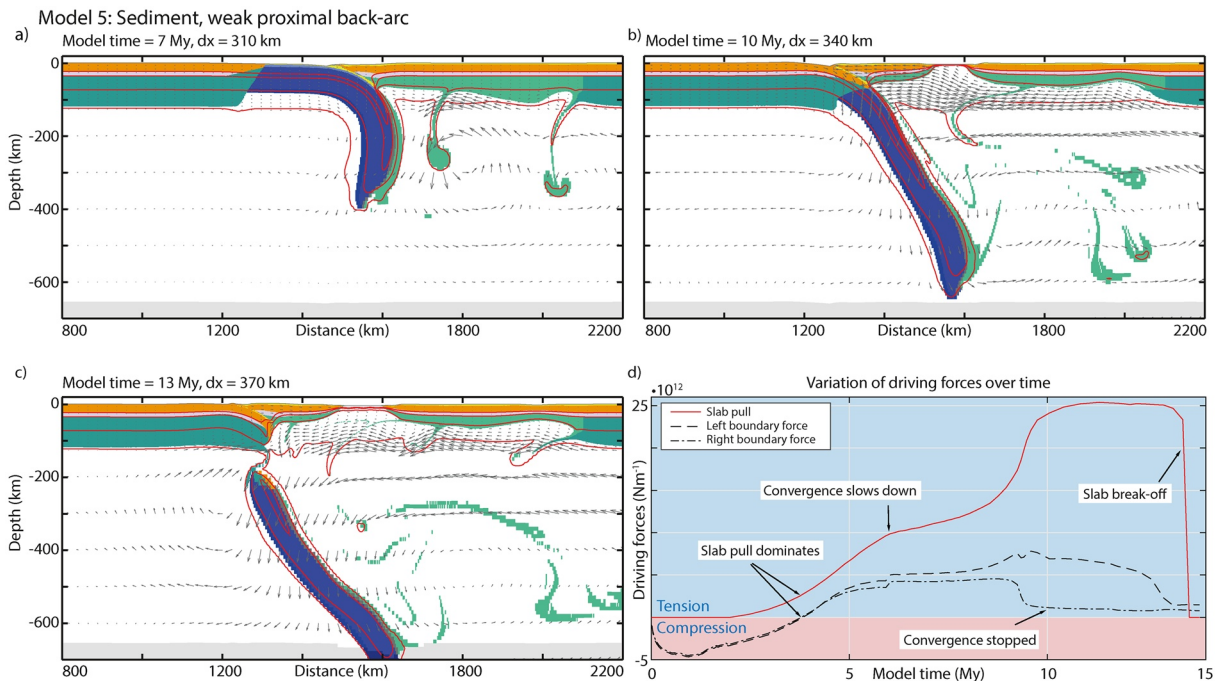


Figure 7. Weak back-arc model with oceanic sediments (Model 5) showing back-arc spreading. (a–c) Material colors (see Figure 1 and legend there) of key time steps, with isotherms (red lines: 420°C, 550°C, 900°C, and 1,330°C) and advection velocities (gray arrows; lengths scale with velocities). (d) Driving force estimates throughout the model run.

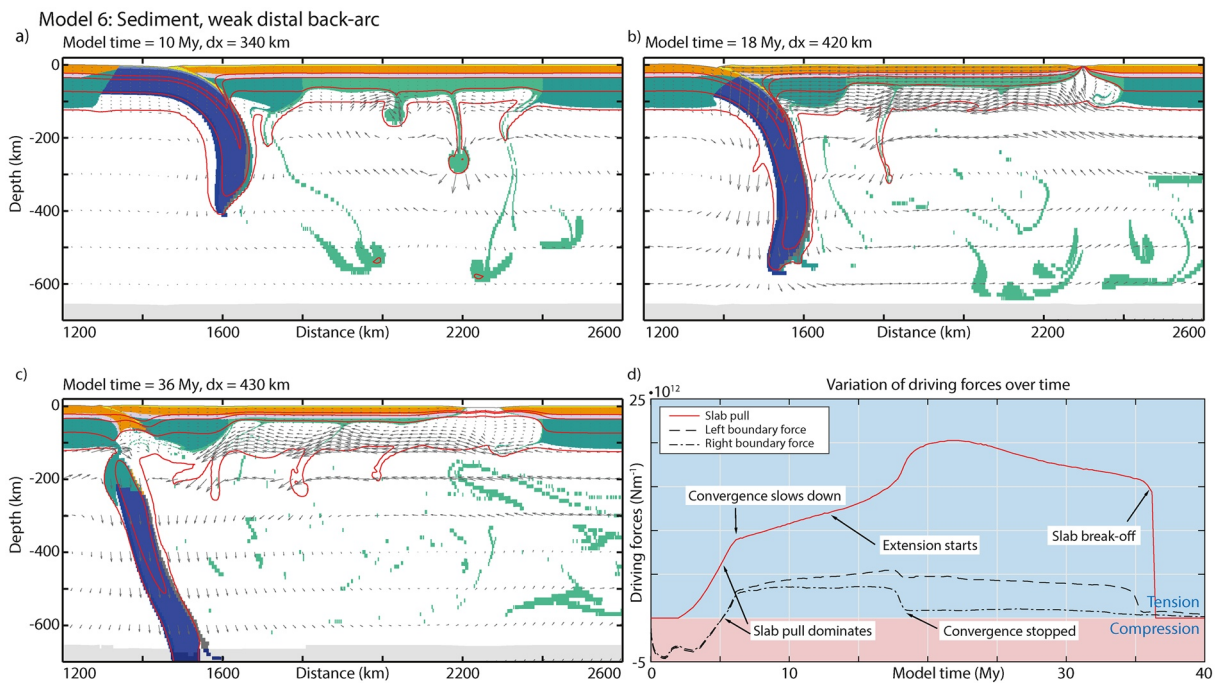


Figure 8. Model with weak distal backarc and oceanic sediments (Model 6) showing distal back-arc breakup. (a–c) Material colors (see Figure 1 and legend there) of key time steps, with isotherms (red lines: 420°C, 550°C, 900°C, and 1,330°C) and advection velocities (gray arrows; lengths scale with velocities). (d) Driving force estimates throughout the model run.

full lithospheric breakup by 9.5 Myr rather than the 13 Myr observed in Model 2 (Figure 7b). Convergence is stopped already at 10 Myr as the oceanic basin is closed. Back-arc breakup occurs somewhat further away from the subduction zone, and the portion torn off of the overriding plate by the largely symmetrical rift is about 260-km wide. The rift reaches its maximum width of approximately 210 km by 12 Myr. At around 13.4 Myr, the slab hanging in a subvertical position breaks off from the procontinent at the bottom of the lithosphere (Figure 7c).

The evolution of the driving forces is plotted in Figure 7d. The evolution of the slab-pull force is very similar to that of Model 2 (Figure 4d), but it reaches its peak value of $2.5 \times 10^{13} \text{ N m}^{-1}$ already at 10 Myr model time; 5 Myr earlier than Model 2. In this model, the backarc starts to extend earlier (at around 6.6 Myr) and the slab starts rolling back earlier as well. The evolution of the tectonic forces also resembles that of Model 2 with similar values but with everything from the point where slab-pull starts dominating the system happening significantly earlier.

3.6. Model 6: Weak Distal Backarc and Weak Plate Interface

The most notable difference between the corresponding models of the two sets can be observed in case of the distal weak zone experiments (Model 3 and Model 6). Model 6 that includes oceanic sediments exhibits back-arc extension (Figure 8, Supporting information Figure S6, and Supporting information Animation 6), whereas Model 3 does not.

Distributed extension of the overriding plate starts around 10 Myr (as the slab reaches around 400 km depth; Figure 8a) and is followed by localized back-arc breakup around 18.3 Myr, when a discrete, symmetric continental rift is formed at the distal edge of the weak zone (Figure 8b). Even though convergence is stopped, and the initial oceanic basin is fully subducted at 19 Myr, there is some continued convergence between the now static proplate and the arc block. The continued extension in the back-arc region results in the formation of an approximately 200-km-wide rift at around 24 Myr (see Supporting information Animation 6).

Soft docking is followed by a period during which the slab gradually retreats further below the procontinent, slowly exposing the subduction interface to the asthenosphere (see Supporting information Animation 6). Finally, at around 36 Myr model time, the slab breaks off at the base of the lithosphere, triggering rapid uplift, retrograde drift of the arc region, and closing of the back-arc basin (see Figure 8c).

The evolution of the driving forces is plotted in Figure 8d. In this model, slab-pull starts dominating the system at approximately 5 Myr model time (Figure 8d). Unlike in case of Model 3, where the tensional forces measured on the boundaries remain close to zero, the same forces here reach values around $3\text{--}4 \times 10^{12} \text{ N m}^{-1}$. These increased values point to less energy dissipation along the slab interface. The high tensional forces measured along the right boundary infer an efficient transfer of the slab-pull force into the overriding plate, which is key in overcoming the decreasing integrated strength of the backarc. Unlike in Model 3, here the backarc starts extending at around 13 Myr model time, allowing for the slab to roll back and the slab-pull force to reach a peak value of $2 \times 10^{13} \text{ N m}^{-1}$ approximately 2 Myr after the convergence is stopped, as the slab reaches a near vertical position. From this point onwards, the slab-pull gradually decreases as the slab heats up before it breaks off at approximately 36 Myr. When the breakup occurs at around 18.3 Myr the tectonic forcing on the right boundary drops to a near zero value inferring a decoupling between the two sides of the system. The boundary force measured along the left side boundary remains in the region of $5 \times 10^{12} \text{ N m}^{-1}$ until the slab breaks off showing how the plate is still being pulled-on by the vertically hanging slab.

3.7. Lithospheric Thinning and Surface Heat Flow Density

We have tracked the average depth of the $1,200^\circ\text{C}$ isotherm and calculated pre-breakup surface heat flow density profiles along the back-arc region for five of the presented models (Models 1 and 4 produce stable subduction without back-arc thinning, hence their heat flow density and isothermal depth profiles are almost identical; see Supporting information Figure S7).

When the convective thinning of the back-arc mantle–lithosphere is absent (Model 1) the surface heat flow density remains stable along the backarc at a value of approximately 52 mW m^{-2} , while the depth of the $1,200^\circ\text{C}$ deepens very gradually (approximately 3 km in 40 Myr) owing to secular cooling of the model.

Model 3 is the only model that produces back-arc thinning (in the weakened distal zone) but no lithosphere breakup. This results in slightly elevated surface heat flow density values along the weak portion of the backarc ($55\text{--}57 \text{ mW m}^{-2}$), while the average depth of the $1,200^\circ\text{C}$ isotherm is advected up to a depth of approximately 65 km by the time the oceanic basin is consumed.

For models that result in lithosphere breakup (Models 2, 5, and 6), the pre-breakup surface heat flow density profiles vary widely with moderately elevated values ($57\text{--}60 \text{ mW m}^{-2}$) away from the crustal necking zone and elevated ($67\text{--}77 \text{ mW m}^{-2}$) values around the necking zones. Model 5 is an exception with a second zone of lithosphere thinning at the distal end of the weak backarc which results in a second zone of strongly elevated surface heat flow density. The average depth of the $1,200^\circ\text{C}$ isotherm is in the order of 70 km for all three models and is only mildly modified after lithosphere breakup. Note that the average isothermal depth of Model 6 is influenced by the fact that part of the lithosphere necking and breakup zone falls within the computational window.

4. Discussion

4.1. Analysis of Forces Controlling Back-Arc Extension

We first discuss the main driving and resisting forces controlling the dynamics of the subduction arc–back-arc system following earlier work (e.g., Forsyth & Uyeda, 1975; Wolf & Huisman, 2019). The main driving force in the system is the slab-pull force (F_{sp}), which results from the density difference between the subducting slab and the surrounding mantle. In the reference model, slab-pull increases with time and reaches a maximum of $1.5 \times 10^{13} \text{ N m}^{-1}$.

A number of forces work against the slab-pull force. (1) Shear resistance at the interface (F_{if}) can be approximated by its integrated frictional strength:

$$F_{if} = \frac{1}{2} \rho g z_{LAB}^2 \sin \phi_{eff} + C z_{LAB} \cos \phi_{eff} \quad (3)$$

The interface shear force depends on the length and the frictional strength of the interface. The long and strong interface of Models 1 and 3 results in a frictional interface strength $\sim 9.5 \times 10^{12} \text{ N m}^{-1}$, while cases with convective lithosphere thinning at the interface (e.g., Model 2) and/or with subduction of weak sediments (Models 4–6) result in an interface strength as low as $2.5 \times 10^{12} \text{ N m}^{-1}$ for Model 5 where both sediment weakening and convective thinning combine. (2) The internal deformation of the slab through viscous bending (F_{bend}) can be approximated by the following equation (Conrad & Hager, 1999; Funicello et al., 2003):

$$F_{bend} = v_{conv} \mu_{eff} h^3 / r^3 \quad (4)$$

where v_{conv} , μ_{eff} , h , and r are the convergence velocity, the viscosity, the thickness, and the radius of curvature of the slab, respectively. For a very similar modeling setup, Wolf and Huismans (2019) estimated F_{bend} in the order of 5×10^{11} to $5 \times 10^{12} \text{ N m}^{-1}$. (3) The resisting force arising from the buoyancy related to the upper- to lower-mantle phase transition (F_{660}) is estimated to be in the order of $2\text{--}4 \times 10^{12} \text{ N m}^{-1}$ when the slab passes straight through the phase transition (Wolf & Huismans, 2019). However, this force will have very little impact on the models presented here as the oceanic lithosphere is consumed by the time its tip reaches the phase transition. (4) Viscous drag along the surface of the slab in the mantle (F_{vd}) is estimated in our models following Billen (2008) (see also Wolf & Huismans, 2019) using:

$$F_{vd} = \frac{2 v_{conv}}{w} \mu_{ml} L \quad (5)$$

where convergence velocity is $v_{conv} \sim 5 \text{ cm year}^{-1}$, viscosity of the mantle is $\mu_{ml} = 1 \times 10^{19}$ to $1 \times 10^{20} \text{ Pa s}$, length of the slab is $L = 600 \text{ km}$, and the length scale for the boundary layer accommodating the shear is $w = 100 \text{ km}$ (after Billen, 2008). These values lead to a viscous drag force along the slab of approximately $2 \times 10^{11} \text{ N m}^{-1}$, very small compared to slab-pull. (5) The integrated strength of the overriding plate is also there to resist the portion of the slab-pull force transmitted into the plate. Here, it is calculated as a depth integral of the minimum of the plastic yield stress and the viscous yield stress. For a strong overriding plate rheology, its value is stable at approximately $8.5 \times 10^{12} \text{ N m}^{-1}$. For a weak back-arc setup, the initial strength is approximately $4 \times 10^{12} \text{ N m}^{-1}$ but as the mantle–lithosphere gets convectively removed this value decreases to as low as $1 \times 10^{12} \text{ N m}^{-1}$ (e.g., by the end of Model 3).

These estimates suggest that the net available driving force for back-arc extension is given by slab-pull force, F_{sp} , modulated by the subduction interface force, F_{if} , here $F_{sp} - F_{if} \sim 5 \times 10^{12} \text{ N m}^{-1}$. For the reference model, this is insufficient to overcome the integrated strength of the overriding plate. However, in cases with convective removal of back-arc mantle–lithosphere, the available driving force is sufficient to overcome the reduced integrated strength of the overriding plate. Similarly, cases of reduced interface resistance lead to an increase of the net driving force available for overriding plate extension.

Some previous numerical modeling studies suggest that viscous drag along the base of the overriding plate lithosphere controls the back-arc stress field (e.g., Capitanio et al., 2011; Dal Zilio et al., 2018; Holt et al., 2015; Sleep & Toksoz, 1971; Suchoy et al., 2021). The basal drag force in our models is following Billen (2008) approximated by

$$F_{bd} = \frac{2 v_{diff}}{w} \mu_{ml} L_{op} \quad (6)$$

where $v_{diff} \sim 5 \text{ cm year}^{-1}$ is the velocity difference between overriding plate and the underlying mantle, $\mu_{ml} \sim 1 \times 10^{19}$ to $1 \times 10^{20} \text{ Pa s}$ the viscosity of the upper mantle at the LAB, $L_{op} \sim 1,500 \text{ km}$ the width of the overriding plate, and the same length scale related to the velocity difference that was used for estimating F_{vd} ($L_{op} = 100 \text{ km}$; after Billen, 2008). With these numbers, the viscous drag force is in the range of 1.5×10^{11} to $1.5 \times 10^{12} \text{ N m}^{-1}$. Compared to the estimates of slab-pull and interface resistance, viscous drag is thus unlikely to play a critical role influencing the back-arc stress field in our models. It should be noted that with

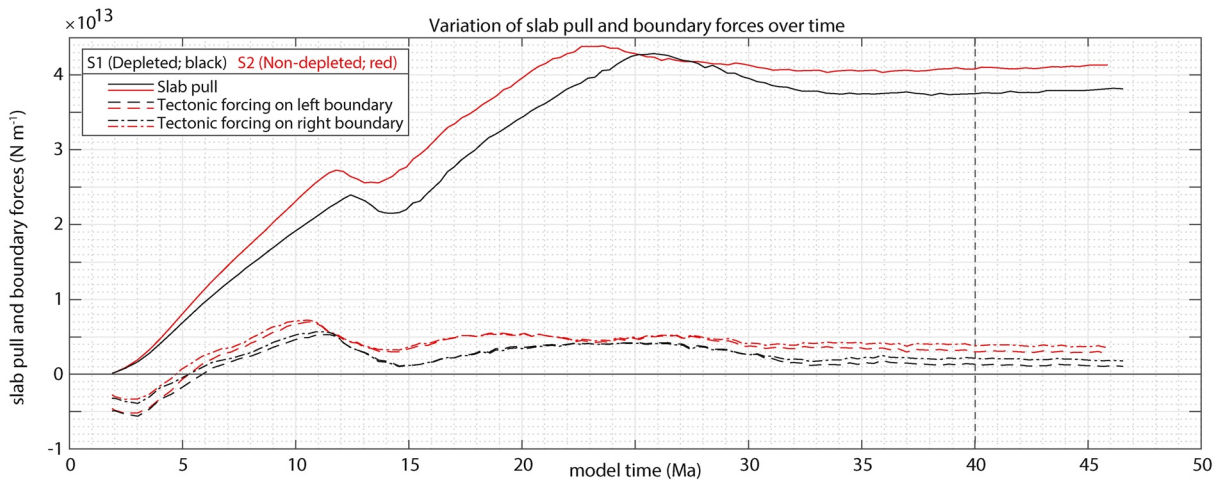


Figure 9. Variation of slab-pull force and tectonic boundary forces over time calculated for the Supporting information Models S1 and S2. The vertical dashed line at 40 Myr years marks where we have taken representative values presented in the text.

higher viscosities in the sublithospheric mantle and larger plates, viscous drag can become a significant actor (e.g., Dal Zilio et al., 2018; Suchoy et al., 2021).

In order to evaluate the transfer of slab-pull into the overriding plate, we have run two additional models with convergence velocity $v_{\text{conv}} = 5 \text{ cm year}^{-1}$ and no incoming plate (see Supporting information Model Animations S1 and S2). In Model S1, we use the same oceanic lithosphere as in models above while in Model S2 the depleted part of the oceanic lithosphere is replaced with nondepleted higher density material. Model S2 results in an increased slab-pull force transmitted to the overriding plate. In both models, the peak tension on the right edge of the overriding plate is reached at around 10–12 Myr with a peak value of approximately $5.8 \times 10^{12} \text{ N m}^{-1}$ for S1 and $7 \times 10^{12} \text{ N m}^{-1}$ for S2 before the slab penetrates the 660 km phase transition zone. The models reach quasi steady state subduction after 35 Myr (Figure 9). At 40 Myr, the slab-pull in Model S2 with denser oceanic lithosphere is $3.3 \times 10^{12} \text{ N m}^{-1}$ higher compared to Model S1, corresponding to a tensional force on the side boundary in Model S2 that is of $1.6 \times 10^{12} \text{ N m}^{-1}$ higher compared to Model S1 (Figure 9). That a change in slab-pull leads to a corresponding change in tension in the overlying plate demonstrates that a significant portion of the slab-pull force is transmitted through the interface.

We closely examine the stress field of the overriding plate lithosphere of Model S1 (Figure 10). The depth-integrated horizontal deviatoric stress (a proxy for the horizontal force) is constant at $1.8 \times 10^{12} \text{ N m}^{-1}$ and tensional for most of the overriding plate (Figure 10a). The horizontal force only becomes compressional within a short distance to the subduction zone (Figure 10a) as also shown by the distribution of the horizontal deviatoric stress field (Figure 10b) with compressional stresses only locally present in the arc region. We computed the smallest principal deviatoric stress component, τ_3 , which is dominantly horizontal in the overriding plate (Figure 10c). However, in the vicinity of the subduction zone, the stress-pattern becomes increasingly complex with prominent rotation of τ_3 to a direction perpendicular to the subduction interface. The deformation in the area above the subduction zone is affected both by downward bending and by shearing along the subduction interface. The rotation of the principal stress directions, overall compressional stresses, and downward bending of the overriding plate in the vicinity of the subduction zone are a result of local shearing along the interface and downward bending of the overriding plate resulting from the slab pulling down in a vertical direction. The length scale of the transition from a tensional to a compressional stress state and the near-absence of deviatoric stresses along the base of the overlying plate lithosphere support our inference that viscous basal drag plays a negligible role in shaping the stress field of the overriding plate in our experiments. The tensional stress state in the overriding plate in our experiments is mainly controlled by the slab-pull force transmitted through the subduction interface.

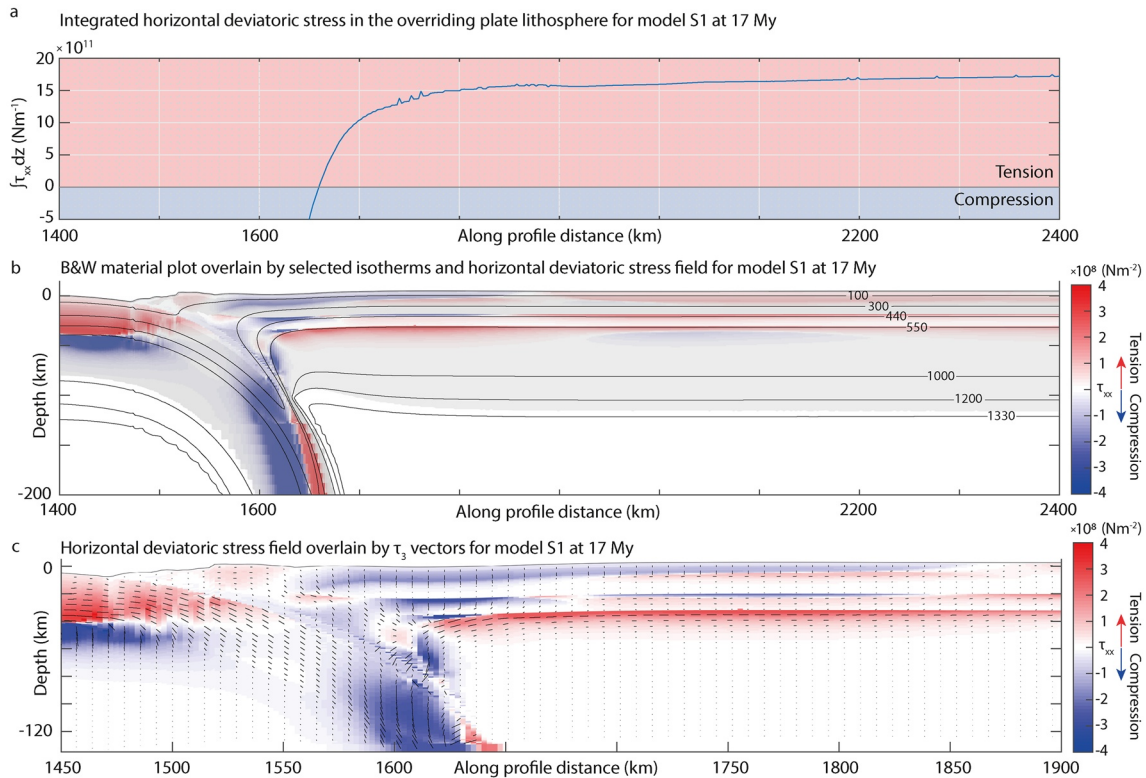


Figure 10. Stress state of the overriding plate lithosphere of Model S1 at 17 Myr. (a) Integrated horizontal deviatoric stress in the overriding plate. When the curve is in the red (positive) domain the overall horizontal deviatoric stress field is tensional while when the curve is in the blue (negative) domain the overall horizontal deviatoric stress field is compressional. (b) Selected isotherms (black lines; contour labels in $^{\circ}\text{C}$) and the horizontal deviatoric stress field (τ_{xx}) plotted on top of the black and white material plot. Positive values (red) correspond to tension while negative values (blue) correspond to compression. (c) Extract of the horizontal deviatoric stress field (τ_{xx}) overlain by the minimum principal stress component (τ_3). The length of the bars represents the local magnitude, while the direction of the bars represents the local orientation of the minimum principal stress component. Note the different scale between (b) and (c).

4.2. Analysis of Model Behavior

The implications of our results and force-balance analysis can be best understood in the context of the main driving and resisting forces for subduction and back-arc extension. Slab-pull is the primary factor driving subduction and back-arc extension in our models, while back-arc lithosphere-integrated strength and shear resistance of the subduction interface are the primary factors resisting back-arc extension. We summarize below in four contrasting cases how these factors interact and control the existence of back-arc extension.

In Case 1, the slab-pull is never sufficiently high to overcome the combined effect of the high integrated strength of the unperturbed backarc and the high frictional strength of the subduction interface (Figure 11) resulting in stable long-term subduction. Model 1 with $F_{sp} \sim 1.5 \times 10^{13} \text{ N m}^{-1}$, interface resistance $F_{if} \sim 9.5 \times 10^{12} \text{ N m}^{-1}$, and overlying plate strength $F_{is} \sim 8.5 \times 10^{12} \text{ N m}^{-1}$ provides an example of Case 1 behavior, with $F_{sp} < F_{if} + F_{is}$.

In Case 2, the slab-pull is similar to Case 1, while the integrated strength of the backarc diminishes with the convective removal of its mantle–lithosphere. The resulting corner flow also reduces the length of the interface, effectively reducing its integrated strength and the energy dissipated along it (Figure 11). As a result, the slab-pull force is now sufficient to overcome the reduced back-arc strength, resulting in overriding plate extension and trench retreat. Model 2 with $F_{sp} \sim 1.2 \times 10^{13} \text{ N m}^{-1}$, a reduced interface resistance $F_{if} \sim 4 \times 10^{12} \text{ N m}^{-1}$, and overlying plate strength $F_{is} \sim 3.5 \times 10^{12} \text{ N m}^{-1}$ (at the onset of extension) provides an example of Case 2 behavior, with $F_{sp} > F_{if} + F_{is}$.

In Case 3, a strong mantle–lithospheric block separates the subduction interface from the weak backarc. Buildup of the slab-pull force and the decrease in the integrated strength of the backarc is very similar to

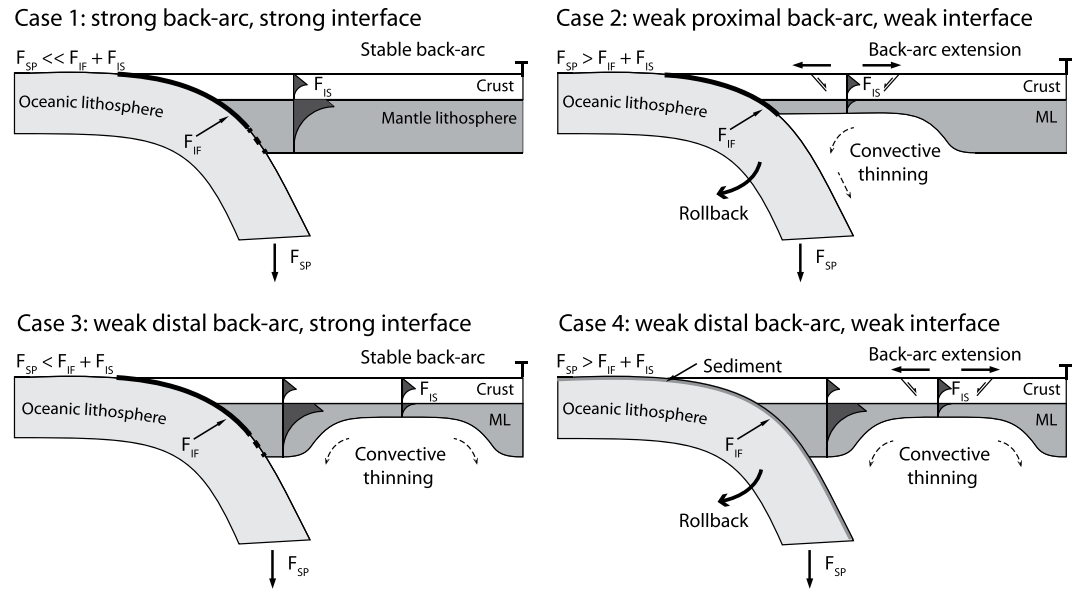


Figure 11. Generalized cartoons of the presented key models showing the effect of weak overriding plate mantle–lithosphere (a, b) and the effect of a weak subduction interface (c, d). Case 1 corresponds to Model 1; Case 2 corresponds to Model 2; Case 3 corresponds to Model 3; and Case 4 corresponds to Model 6.

that of Case 2, but the subduction interface remains long and strong, hence the energy dissipation along it remains significant. In this scenario, the slab-pull is insufficient to overcome the combined effect of the low integrated strength of the backarc and the high-energy dissipation along the interface. This case is illustrated by Model 3 that even though its back-arc lithosphere is weakened to $F_{is} \sim 3.5 \times 10^{12} \text{ N m}^{-1}$ (at the time of maximum slab-pull: $F_{sp} \sim 1 \times 10^{13} \text{ N m}^{-1}$), slab-pull cannot overcome the combined effects of interface ($F_{if} \sim 9.5 \times 10^{12} \text{ N m}^{-1}$) and overlying plate strength, for example, $F_{sp} < F_{if} + F_{is}$. As a result, there is no back-arc extension in the corresponding model.

Case 4 presents a scenario in which the length of the interface remains constant through time, but the strength of the interface is reduced as weak sediments subduct on top of the oceanic plate. In this scenario, the gradually increasing slab-pull becomes high enough over time, to overcome the combined strength of the weak subduction interface and the gradually decreasing strength of the convectively thinned overriding plate, resulting in back-arc extension and rifting. Model 6 with a slab-pull value of $F_{sp} \sim 1.25 \times 10^{13} \text{ N m}^{-1}$ at the start of extension, a low interface resistance resulting from sediment subduction with $F_{if} \sim 7 \times 10^{12} \text{ N m}^{-1}$, and overlying plate strength weakened by convective removal with $F_{is} \sim 3.5 \times 10^{12} \text{ N m}^{-1}$ (at the onset of extension) provides an example of Case 4 behavior, where $F_{sp} > F_{if} + F_{is}$.

The role of sediment subduction in weakening the interface is especially notable as it allows transfer of a higher portion of the slab-pull force into the backarc as illustrated by the difference in tensional force in the overriding plate between Models 3 and 6 (e.g., Figures 5 and 8d). In Model 3, without sediment subduction and reference interface strength, the tensional force in the overriding plate remains close to 0 throughout the model evolution while in Model 6 with sediment subduction along the interface the tensional force in the overriding plate reaches $3.5 \times 10^{12} \text{ N m}^{-1}$ when slab-pull dominates the system. The same effect is present in the other models. In models with a strong back arc lithosphere (Model 1 and Model 4, Figures 3d and 6b), the difference between the tensional force in the overriding plate is in the order of $2.5 \times 10^{12} \text{ N m}^{-1}$. For models with convective removal of the mantle–lithosphere in the mantle wedge that shortens the subduction interface (Model 2 and Model 5, Figures 4 and 7d), the difference in overlying plate tension is lower, approximately $0.5 \times 10^{12} \text{ N m}^{-1}$. For these latter two models, the interface strength is affected by the convective removal of the overriding plate mantle–lithosphere, which shortens the interface over time, limiting its overall effect on the system. These values point to a systematic behavior, whereby the lower energy dissipation along the subduction interface owing to the lubricating effect of weak subducting material results in

a higher portion of the slab-pull force to be transferred into the overriding plate, where the strength of the effect depends on the length of the interface itself.

4.3. Implications and Comparison With Previous Studies

Our results show that the presence of a weak mantle–lithospheric zone near the subduction interface lowers the integrated strength of the backarc in three main ways: (1) by thinning, (2) by thermal weakening of the lithosphere, and (3) by reducing the length of the subduction interface. Wolf and Huismans (2019) provided an estimate of the force balance for a very similar experimental setup. They argue for the crucial role of a weak overriding plate rheology that leads to convective thinning and back-arc weakening in order to achieve back-arc extension and the models presented here are in agreement with their results.

The existence of such preexisting weak mantle–lithospheric zones can be explained by—for example—(a) fluid infiltration from the subducting plate (e.g., Arcay et al., 2006) or (b) an anomalously high geothermal gradient, owing to enhanced crustal radioactive heat production or high transient temperatures associated with an episode of lithosphere thickening and associated radioactive self-heating (e.g., Currie et al., 2008) and (c) inherited lithospheric weakness resulting from earlier tectonic deformation or terrain accretion during long lasting subduction as observed over most of the Tethyan belt. Currie et al. (2008) argued that thinning of overriding mantle–lithosphere over a wider zone can also be explained by a higher compositional density or a hotter initial thermal structure.

Our results also show that the low-strength sedimentary material lubricates the subduction zone, resulting in less energy dissipating along the subduction interface, and transmission of a larger portion of the slab-pull into the overriding plate. The lubricating effect of oceanic sediments has also been suggested as an explanation for the along-strike variations in topographic evolution of the Andes (e.g., Lamb, 2006). Moreover, Sobolev and Brown (2019) argued that the rise of continents and the accumulation of weak sediments at continental edges and in trenches has allowed for establishment of a stable subduction regime on Earth, contributing to the emergence of plate tectonics itself. The models presented here show that the rheology of the subduction interface is one of the controlling factors in the development of back-arc extension consistent with earlier model inferences (e.g., De Franco et al., 2007).

5. Comparison With Nature

The models presented here also exhibit a range of first-order features characteristic of natural extensional back-arc systems. The modeling setup chosen is inspired by and corresponds well to Mediterranean style arc-back-arc systems where the rate of convergence is low owing to the slow convergence of Africa and Europe, and the amount of oceanic lithosphere is limited (Faccenna et al., 1997, 2014; Jolivet & Faccenna, 2000; L. Royden & Faccenna, 2018).

Our models show that back-arc extension and breakup in such a narrow and restricted system is viable when the overriding plate lithosphere is sufficiently weak. The modeled time scale of extension (3–6 Myr from the start of crustal extension to breakup) is also compatible with observations from the Mediterranean region (e.g., Faccenna et al., 2014; Magni et al., 2013, 2014). The presence of a sedimentary layer on top of the oceanic lithosphere (ubiquitous in the Mediterranean oceanic basins) facilitates extension in the back-arc region as shown here.

The initial width of the oceanic basin (500 km) in the models presented here represent the lower range of the amount of oceanic subduction inferred for the Mediterranean region (400–1,000 km; e.g., Faccenna et al., 2014). The amount of trench retreat for our models with back-arc breakup varies between 200 km (Model 6) and 260 km (Model 5). These values are consistent with the lower range of trench retreat inferred for the Mediterranean (Faccenna et al., 2014). The type of rifting produced by the models is predominantly narrow and symmetrical while those observed in the Mediterranean region range from narrow, to wide, and in some cases core-complex style deformation (Faccenna et al., 1997).

In particular, the large-scale evolution of Model 2 compares favorably with observations from the North Tyrrhenian Sea (Figure 1b; Diaferia et al., 2019; Doglioni et al., 1999; Piana Agostinetti & Faccenna, 2018) with its moderately thinned back-arc crust (20–30-km thick) adjacent to the subducting Adriatic slab and

its extremely thinned mantle–lithosphere that exhibit anomalously high Moho temperatures (LAB depth of 60 km below the North Tyrrhenian basin). Extension of the backarc started in the Late Miocene (e.g., Patacca et al., 1990) with different extension rates for the northern and the southern part of the basin, with an approximately 300 km of subduction trench retreat in the northern part comparable to Model 2.

In turn, the evolution of Model 6 compares favorably to many aspects of the evolution of the Pannonian basin (Figure 1a). The 11 Myr time frame estimated for the back-arc extension is comparable to the time between the onset of extension and crustal breakup of Model 6. The basin experienced wide-spread crustal thinning that—unlike the extremely thinned mantle–lithosphere—our models do not reproduce. In addition, the undeformed proximal area resembles the largely unextended Transylvanian region with its comparatively thicker postrift lithospheric root. Given its position adjacent to the subduction zone, this root would be expected to be more vulnerable for subduction erosion and ablation by the corner flow. This appears not to have affected the Transylvanian block suggesting higher nominal lithospheric strength. There is furthermore, volcanological evidence supporting sediment subduction along the Carpathian subduction zone (e.g., Jurje et al., 2013) that may have weakened the subduction interface allowing for a more efficient transfer of the slab-pull into the backarc as in our Model 6.

6. Conclusions

In this paper, we use two-dimensional numerical model experiments to investigate how overriding plate rheology and strength of the subduction interface affect the closure of narrow land-locked ocean basins and extension in the back-arc region. We conclude the following.

1. Our models and simple force-balance arguments show that two factors work in tandem to facilitate back-arc extension in small land-locked oceanic basins such as observed in the Mediterranean. (I) Back-arc weakening by convective removal of mantle–lithosphere reducing the strength of the overriding plate. (II) Weakening of the subduction interface.
2. Subduction interface weakening may occur in two different ways. (I) By thinning of the mantle–lithosphere in the mantle wedge area close to the subduction zone that reduces the length of the subduction interface and therefore lowers the energy dissipated. (II) Subduction of weak sediment on top of the oceanic lithosphere weakening the subduction interface. In settings where back-arc lithosphere thinning occurs far from the subduction zone, weakening of the subduction interface by other processes such as sediment subduction appears paramount.
3. A detailed analysis of the overriding plate stress field showed that the slab-pull force transmitted through the subduction interface has a prominent role in driving back-arc extension while the viscous drag acting along the base of the lithosphere has a negligible role in our experiments.
4. The North Tyrrhenian subduction zone is characterized by extremely thin back-arc mantle–lithosphere up to the mantle wedge and a narrow zone of back-arc extension. Our model results suggest that back-arc mantle–lithosphere thinning up to the mantle wedge has facilitated slab roll back and back-arc extension of the North Tyrrhenian subduction zone.
5. The Pannonian basin is characterized by removal of the back-arc mantle–lithosphere far behind the subduction zone with the strong Transylvanian block of thick back-arc lithosphere in the area adjacent to the subduction zone and ample evidence of sediment subduction along the East Carpathians. Our models provide an explanation for how limited slab-pull associated with the closure of a small land-locked oceanic basin and subduction beneath the East Carpathians may have worked in tandem with a sediment filled weak subduction interface and convective thinning beneath the Pannonian basin allowing back-arc extension.

Data Availability Statement

No new data were used for this study. Parameter values used to produce the numerical model results are provided in Table 1.

Acknowledgments

This work has been carried out by the financial support of the Hungarian National Research Fund project OTKA-K120149. We thank Uninett Sigma2 for computing time of project NN4704K. We also thank Anthony Jourdon and an anonymous reviewer for their constructive comments on the manuscript.

References

- Agursta, R., Goes, S., & van Hunen, J. (2017). Subducting-slab transition-zone interaction: Stagnation, penetration and mode switches. *Earth and Planetary Science Letters*, *467*, 10–23. <https://doi.org/10.1016/j.epsl.2017.02.005>
- Angiboust, S., Agard, P., Raimbourg, H., Yamato, P., & Huet, B. (2011). Subduction interface processes recorded by eclogite-facies shear zones (Monviso, W. Alps). *Lithos*, *127*, 222–238. <https://doi.org/10.1016/j.lithos.2011.09.004>
- Arcay, D., Doin, M. P., Tric, E., Bousquet, R., & de Capitani, C. (2006). Overriding plate thinning in subduction zones: Localized convection induced by slab dehydration. *Geochemistry, Geophysics, Geosystems*, *7*, Q02007. <https://doi.org/10.1029/2005GC001061>
- Balázs, A., Matenco, L., Magyar, I., Horváth, F., & Cloetingh, S. (2016). The link between tectonics and sedimentation in back-arc basins: New genetic constraints from the analysis of the Pannonian Basin. *Tectonics*, *35*, 1526–1559. <https://doi.org/10.1002/2015TC004109>
- Beaumont, C., Nguyen, M. H., Jamieson, R. A., & Ellis, S. (2006). Crustal flow modes in large hot orogens. *Geological Society, London, Special Publications*, *268*, 91–145. <https://doi.org/10.1144/gsl.sp.2006.268.01.05>
- Behr, W. M., & Becker, T. W. (2018). Sediment control on subduction plate speeds. *Earth and Planetary Science Letters*, *502*, 166–173. <https://doi.org/10.1016/j.epsl.2018.08.057>
- Billen, M. I. (2008). Modeling the dynamics of subducting slabs. *Annual Review of Earth and Planetary Sciences*, *36*, 325–356. <https://doi.org/10.1146/annurev.earth.36.031207.124129>
- Billen, M. I. (2010). Slab dynamics in the transition zone. *Physics of the Earth and Planetary Interiors*, *183*, 296–308. <https://doi.org/10.1016/j.pepi.2010.05.005>
- Bos, B., & Spiers, C. J. (2002). Frictional-viscous flow of phyllosilicate-bearing fault rock: Microphysical model and implications for crustal strength profiles. *Journal of Geophysical Research*, *107*(B2), 2028. <https://doi.org/10.1029/2001JB000301>
- Butler, J. P., & Beaumont, C. (2017). Subduction zone decoupling/retreat modeling explains south Tibet (Xigaze) and other supra-subduction zone ophiolites and their UHP mineral phases. *Earth and Planetary Science Letters*, *463*, 101–117. <https://doi.org/10.1016/j.epsl.2017.01.025>
- Butler, J. P., Beaumont, C., & Jamieson, R. A. (2015). Paradigm lost: Buoyancy thwarted by the strength of the Western Gneiss Region (ultra)high-pressure terrane, Norway. *Lithosphere*, *7*, 379–407. <https://doi.org/10.1130/L426.1>
- Capitanio, F. A., Faccenna, C., Zlotnik, S., & Stegman, D. R. (2011). Subduction dynamics and the origin of Andean orogeny and the Bolivian orocline. *Nature*, *480*, 83–86. <https://doi.org/10.1038/nature10596>
- Ciulavu, D., Dinu, C., & Cloetingh, S. A. P. L. (2001). Late Cenozoic tectonic evolution of the Transylvanian basin and northeastern part of the Pannonian basin (Romania): Constraints from seismic profiling and numerical modelling. *Stephan Mueller Special Publication Series*, *3*, 105–120. <https://doi.org/10.5194/smsps-3-105-2002>
- Cloos, M., & Shreve, R. L. (1988a). Subduction-channel model of prism accretion, melange formation, sediment subduction, and subduction erosion at convergent plate margins: 1. Background and description. *Pure and Applied Geophysics*, *128*, 455–500. <https://doi.org/10.1007/BF00874548>
- Cloos, M., & Shreve, R. L. (1988b). Subduction-channel model of prism accretion, melange formation, sediment subduction, and subduction erosion at convergent plate margins: 2. Implications and discussion. *Pure and Applied Geophysics*, *128*, 501–545. <https://doi.org/10.1007/BF00874549>
- Conrad, C. P., & Hager, B. H. (1999). Effects of plate bending and fault strength at subduction zones on plate dynamics. *Journal of Geophysical Research*, *104*, 17551–17571.
- Csontos, L., Nagymarosy, A., Horvath, F., & Kovac, M. (1992). Tertiary evolution of the intra-Carpathian area: A model. *Tectonophysics*, *208*, 221–241. [https://doi.org/10.1016/0040-1951\(92\)90346-8](https://doi.org/10.1016/0040-1951(92)90346-8)
- Currie, C. A., Huismans, R. S., & Beaumont, C. (2008). Thinning of continental backarc lithosphere by flow-induced gravitational instability. *Earth and Planetary Science Letters*, *269*, 436–447. <https://doi.org/10.1016/j.epsl.2008.02.037>
- Currie, C. A., & Hyndman, R. D. (2006). The thermal structure of subduction zone back arcs. *Journal of Geophysical Research*, *111*, B08404. <https://doi.org/10.1029/2005JB004024>
- Dal Zilio, L., Faccenna, M., & Capitanio, F. (2018). The role of deep subduction in supercontinent breakup. *Tectonophysics*, *746*, 312–324. <https://doi.org/10.1016/j.tecto.2017.03.006>
- DeCelles, P. G., Ducea, M. N., Kapp, P., & Zandt, G. (2009). Cyclicity in Cordilleran orogenic systems. *Nature Geoscience*, *2*, 251–257. <https://doi.org/10.1038/ngeo469>
- De Franco, R., Govers, R., & Wortel, R. (2007). Numerical comparison of different convergent plate contacts: Subduction channel and subduction fault. *Geophysical Journal International*, *171*, 435–450. <https://doi.org/10.1111/j.1365-246X.2006.03498.x>
- Diaferia, G., Cammarano, F., & Faccenna, C. (2019). Thermal structure of a vanishing subduction system: An example of seismically-derived crustal temperature along the Italian peninsula. *Geophysical Journal International*, *219*, 239–247. <https://doi.org/10.1093/gji/ggz289>
- Di Stefano, R., Kissling, E., Chiarabba, C., Amato, A., & Giardini, D. (2009). Shallow subduction beneath Italy: Three-dimensional images of the Adriatic–European–Tyrrhenian lithosphere system based on high-quality *P* wave arrival times. *Journal of Geophysical Research*, *114*, B05305. <https://doi.org/10.1029/2008JB005641>
- Doglion, C., Gueguen, E., Harabaglia, P., & Mongelli, F. (1999). On the origin of west-directed subduction zones and applications to the western Mediterranean. *Geological Society, London, Special Publications*, *156*, 541–561.
- Eberhart-Phillips, D., & Reyners, M. (1999). Plate interface properties in the Northeast Hikurangi Subduction Zone, New Zealand, from converted seismic waves. *Geophysical Research Letters*, *26*, 2565–2568. <https://doi.org/10.1029/1999GL900567>
- Faccenna, C., Becker, T. W., Auer, L., Billi, A., Boschi, L., Brun, J. P., et al. (2014). Mantle dynamics in the Mediterranean. *Reviews of Geophysics*, *52*, 283–332. <https://doi.org/10.1002/2013RG000444>
- Faccenna, C., Becker, T. W., Lucente, F. P., Jolivet, L., & Rossetti, F. (2001). History of subduction and back-arc extension in the Central Mediterranean. *Geophysical Journal International*, *145*, 809–820. <https://doi.org/10.1046/j.0956-540x.2001.01435.x>
- Faccenna, C., Davy, P., Brun, J.-P., Funicello, R., Giardini, D., Mattei, M., & Nalpas, T. (1996). The dynamics of back-arc extension: An experimental approach to the opening of the Tyrrhenian Sea. *Geophysical Journal International*, *126*, 781–795. <https://doi.org/10.1111/j.1365-246X.1996.tb04702.x>
- Faccenna, C., Mattei, M., Funicello, F., & Jolivet, L. (1997). Styles of back-arc extension in the Central Mediterranean. *Terra Nova*, *9*, 126–130.
- Fodor, L., Csontos, L., Bada, G., Györfi, I., & Benkovic, L. (1999). Tertiary tectonic evolution of the Pannonian basin system and neighbouring orogens: A new synthesis of palaeostress data. *Geological Society, London, Special Publications*, *156*, 295–334.

- Forsyth, D., & Uyeda, S. (1975). On the relative importance of the driving forces of plate motion. *Geophysical Journal International*, 43, 163–200. <https://doi.org/10.1111/j.1365-246X.1975.tb00631.x>
- Funiciello, F., Morra, G., Regenauer-Lieb, K., & Giardini, D. (2003). Dynamics of retreating slabs: 1. Insights from two-dimensional numerical experiments. *Journal of Geophysical Research*, 108(B4), 2206. <https://doi.org/10.1029/2001JB000898>
- Gleason, G. C., & Tullis, J. (1995). A flow law for dislocation creep of quartz aggregates determined with the molten-salt cell. *Tectonophysics*, 247, 1–23. [https://doi.org/10.1016/0040-1951\(95\)00011-B](https://doi.org/10.1016/0040-1951(95)00011-B)
- Goes, S., Agrusta, R., van Hunen, J., & Garel, F. (2017). Subduction-transition zone interaction: A review. *Geosphere*, 13, 644–664. <https://doi.org/10.1130/Ges01476.1>
- Hacker, B. R. (1996). Eclogite formation and the rheology, buoyancy, seismicity, and H₂O content of oceanic crust. In G. E. Bebout, D. W. Scholl, S. H. Kirby, & J. P. Platt (Eds.), *Subduction top to bottom* (pp. 337–346).
- Hirth, G., & Kohlstedt, D. L. (1996). Water in the oceanic upper mantle: Implications for rheology, melt extraction and the evolution of the lithosphere. *Earth and Planetary Science Letters*, 144, 93–108. [https://doi.org/10.1016/0012-821x\(96\)00154-9](https://doi.org/10.1016/0012-821x(96)00154-9)
- Holt, A. F., Becker, T. W., & Buffett, B. A. (2015). Trench migration and overriding plate stress in dynamic subduction models. *Geophysical Journal International*, 201, 172–192. <https://doi.org/10.1093/gji/ggv011>
- Horváth, F., Bada, G., Szafián, P., Tari, G., Ádám, A., & Cloetingh, S. (2006). Formation and deformation of the Pannonian basin: Constraints from observational data. In D. Gee & R. Stephenson (Eds.), *European lithospheric dynamics* (Vol. 32, pp. 191–206). London: Geological Society of London.
- Huismans, R. S., & Beaumont, C. (2011). Depth-dependent extension, two-stage breakup and cratonic underplating at rifted margins. *Nature*, 473, 74–78. <https://doi.org/10.1038/nature09988>
- Jolivet, L., & Faccenna, C. (2000). Mediterranean extension and the Africa–Eurasia collision. *Tectonics*, 19, 1095–1106. <https://doi.org/10.1029/2000TC900018>
- Jurje, M., Ionescu, C., Hoeck, V., & Kovacs, M. (2013). Geochemistry of Neogene quartz andesites from the Oaş and Gutâi Mountains, eastern Carpathians (Romania): A complex magma genesis. *Mineralogy and Petrology*, 108, 13–32. <https://doi.org/10.1007/s00710-013-0282-6>
- Karato, S., & Wu, P. (1993). Rheology of the upper mantle: A synthesis. *Science*, 260, 771–778. <https://doi.org/10.1126/science.260.5109.771>
- Lamb, S. (2006). Shear stresses on megathrusts: Implications for mountain building behind subduction zones. *Journal of Geophysical Research*, 111, B07401. <https://doi.org/10.1029/2005JB003916>
- Lamb, S., & Davis, P. (2003). Cenozoic climate change as a possible cause for the rise of the Andes. *Nature*, 425, 792–797. <https://doi.org/10.1038/nature02049>
- Le Pichon, X. (1982). Land-locked oceanic basins and continental collision: The Eastern Mediterranean as a case example. In K. J. Hsu (Ed.), *Mountain building processes*, London (pp. 201–211).
- Le Pichon, X., Angelier, J., Osmaston, M. F., & Stegena, L. (1981). The Aegean Sea [and Discussion]. *Philosophical Transactions of the Royal Society A: Mathematical, Physical & Engineering Sciences*, 300, 357–372. <https://doi.org/10.1098/rsta.1981.0069>
- Le Pichon, X., Angelier, J., & Sibuet, J. C. (1982). Plate boundaries and extensional tectonics. *Tectonophysics*, 81, 239–256.
- Mackwell, S. J., Zimmerman, M. E., & Kohlstedt, D. L. (1998). High-temperature deformation of dry diabase with application to tectonics on Venus. *Journal of Geophysical Research*, 103, 975–984. <https://doi.org/10.1029/97JB02671>
- Magni, V., Faccenna, C., van Hunen, J., & Funiciello, F. (2013). Delamination vs. break-off: The fate of continental collision. *Geophysical Research Letters*, 40, 285–289. <https://doi.org/10.1002/grl.50090>
- Magni, V., Faccenna, C., van Hunen, J., & Funiciello, F. (2014). How collision triggers backarc extension: Insight into Mediterranean style of extension from 3-D numerical models. *Geology*, 42, 511–514. <https://doi.org/10.1130/g35446.1>
- Matenco, L., & Radivojević, D. (2012). On the formation and evolution of the Pannonian Basin: Constraints derived from the structure of the junction area between the Carpathians and Dinarides. *Tectonics*, 31, TC6007. <https://doi.org/10.1029/2012TC003206>
- Miller, M. S., & Piana Agostinetti, N. (2012). Insights into the evolution of the Italian lithospheric structure from S receiver function analysis. *Earth and Planetary Science Letters*, 345–348, 49–59. <https://doi.org/10.1016/j.epsl.2012.06.028>
- Oncken, O., Asch, G., Haberland, C., Metchie, J., Sobolev, S., Stiller, M., et al. (2003). Seismic imaging of a convergent continental margin and plateau in the central Andes (Andean Continental Research Project 1996 (ANCORP'96)). *Journal of Geophysical Research*, 108(B7), 2328. <https://doi.org/10.1029/2002JB001771>
- Patacca, E., Sartori, R., & Scandone, P. (1990). Tyrrhenian basin and Apenninic arcs: Kinematic relations since late Tortonian times. *Memorie della Società Geologica Italiana*, 45, 425–451.
- Piana Agostinetti, N., & Faccenna, C. (2018). Deep structure of Northern Apennines Subduction Orogen (Italy) as revealed by a joint interpretation of passive and active seismic data. *Geophysical Research Letters*, 45, 4017–4024. <https://doi.org/10.1029/2018GL077640>
- Pysklywec, R. N., & Beaumont, C. (2004). Intraplate tectonics: Feedback between radioactive thermal weakening and crustal deformation driven by mantle lithosphere instabilities. *Earth and Planetary Science Letters*, 221, 275–292. [https://doi.org/10.1016/s0012-821x\(04\)00098-6](https://doi.org/10.1016/s0012-821x(04)00098-6)
- Royden, L., & Faccenna, C. (2018). Subduction Orogeny and the Late Cenozoic evolution of the Mediterranean arcs. *Annual Review of Earth and Planetary Sciences*, 46, 261–289. <https://doi.org/10.1146/annurev-earth-060115-012419>
- Royden, L. H., Horvath, F., & Burchfiel, B. C. (1982). Transform faulting, extension, and subduction in the Carpathian Pannonian region. *The Geological Society of America Bulletin*, 93, 717–725. [https://doi.org/10.1130/0016-7606\(1982\)93<717:TFEASI>2.0.CO;2](https://doi.org/10.1130/0016-7606(1982)93<717:TFEASI>2.0.CO;2)
- Schmid, S. M., Bernoulli, D., Fügenschuh, B., Matenco, L., Schefer, S., Schuster, R., et al. (2008). The Alpine–Carpathian–Dinaridic orogenic system: Correlation and evolution of tectonic units. *Swiss Journal of Geosciences*, 101, 139–183. <https://doi.org/10.1007/s00015-008-1247-3>
- Shreve, R. L., & Cloos, M. (1986). Dynamics of sediment subduction, melange formation, and prism accretion. *Journal of Geophysical Research*, 91, 10229–10245. <https://doi.org/10.1029/JB091iB10p10229>
- Sibson, R. H. (1990). Conditions for fault-valve behavior. *Geological Society - Special Publications*, 54, 15–28.
- Sleep, N., & Toksoz, M. N. (1971). Evolution of marginal basins. *Nature*, 233, 548–550. <https://doi.org/10.1038/233548a0>
- Sobolev, S. V., & Babeyko, A. Y. (2005). What drives orogeny in the Andes? *Geology*, 33, 617. <https://doi.org/10.1130/g21557.1>
- Sobolev, S. V., & Brown, M. (2019). Surface erosion events controlled the evolution of plate tectonics on Earth. *Nature*, 570, 52–57. <https://doi.org/10.1038/s41586-019-1258-4>
- Suchoy, L., Goes, S., Maunder, B., Garel, F., & Davies, R. (2021). Effects of basal drag on subduction dynamics from 2D numerical models. *Solid Earth*, 12, 79–93. <https://doi.org/10.5194/se-12-79-2021>
- Suhadolc, P., Panza, G. F., & Mueller, S. (1990). Physical-properties of the lithosphere asthenosphere system in Europe. *Tectonophysics*, 176, 123–135. [https://doi.org/10.1016/0040-1951\(90\)90262-7](https://doi.org/10.1016/0040-1951(90)90262-7)

- Tao, W. C., & O'Connell, R. J. (1992). Ablative subduction: A two-sided alternative to the conventional subduction model. *Journal of Geophysical Research*, *97*, 8877–8904. <https://doi.org/10.1029/91JB02422>
- Taylor, B., & Karner, G. D. (1983). On the evolution of marginal basins. *Reviews of Geophysics*, *21*, 1727–1741. <https://doi.org/10.1029/RG021i008p01727>
- Tetreault, J. L., & Buitter, S. J. H. (2012). Geodynamic models of terrane accretion: Testing the fate of island arcs, oceanic plateaus, and continental fragments in subduction zones. *Journal of Geophysical Research*, *117*, B08403. <https://doi.org/10.1029/2012JB009316>
- Thieulot, C. (2011). FANTOM: Two- and three-dimensional numerical modeling of creeping flows for the solution of geological problems. *Physics of the Earth and Planetary Interiors*, *188*, 47–68. <https://doi.org/10.1016/j.pepi.2011.06.011>
- Toksöz, M. N., & Hsui, A. T. (1978). Numerical studies of back-arc convection and the formation of marginal basins. *Tectonophysics*, *50*, 177–196. [https://doi.org/10.1016/0040-1951\(78\)90134-8](https://doi.org/10.1016/0040-1951(78)90134-8)
- Tosi, N., Yuen, D. A., de Koker, N., & Wentzcovitch, R. M. (2013). Mantle dynamics with pressure- and temperature-dependent thermal expansivity and conductivity. *Physics of the Earth and Planetary Interiors*, *217*, 48–58. <https://doi.org/10.1016/j.pepi.2013.02.004>
- Tsuru, T., Park, J.-O., Miura, S., Kodaira, S., Kido, Y., & Hayashi, T. (2002). Along-arc structural variation of the plate boundary at the Japan Trench margin: Implication of interplate coupling. *Journal of Geophysical Research*, *107*(B12), 2357. <https://doi.org/10.1029/2001JB001664>
- Vannucchi, P., Sage, F., Phipps Morgan, J., Remitti, F., & Collot, J.-Y. (2012). Toward a dynamic concept of the subduction channel at erosive convergent margins with implications for interplate material transfer. *Geochemistry, Geophysics, Geosystems*, *13*, Q02003. <https://doi.org/10.1029/2011GC003846>
- Warren, C. J., Beaumont, C., & Jamieson, R. A. (2008). Modeling tectonic styles and ultra-high pressure (UHP) rock exhumation during the transition from oceanic subduction to continental collision. *Earth and Planetary Science Letters*, *267*, 129–145. <https://doi.org/10.1016/j.epsl.2007.11.025>
- Wolf, S. G., & Huisman, R. S. (2019). Mountain building or backarc extension in ocean-continent subduction systems: A function of backarc lithospheric strength and absolute plate velocities. *Journal of Geophysical Research: Solid Earth*, *124*, 7461–7482. <https://doi.org/10.1029/2018JB017171>